國立臺灣大學工學院機械工程學系

碩士論文

Department of Mechanical Engineering

College of Engineering

National Taiwan University

Master's Thesis

流固耦合垂盪圓柱之自適應回饋控制

Adaptive feedback flow control of a circular cylinder plunging under flow-structure interaction

劉哲維

Che-Wei Liu

指導教授: 蔡協澄 博士

Advisor: Hsieh-Chen Tsai Ph.D.

中華民國 114 年 7 月

July, 2025

doi:10.6342/NTU202503926

國立臺灣大學碩士學位論文
口試委員會審定書
MASTER'S THESIS ACCEPTANCE CERTIFICATE
NATIONAL TAIWAN UNIVERSITY

流固耦合垂盪圓柱之自適應回饋控制

Adaptive feedback flow control of a circular cylinder plunging under flow-structure interaction

本論文係劉哲維(R12522116)在國立臺灣大學機械所完成之碩士學位論文，於民國 114 年 7 月 25 日承下列考試委員審查通及口試及格，特此證明。

The undersigned, appointed by the Department / Graduate Institute of Mechanical Engineering on 25. 07. 2025 have examined a Master's Thesis entitled above presented by Che-Wei Liu, R12522116 candidate and hereby certify that it is worthy of acceptance.

口試委員 Oral examination committee:

蔡協燉　李宇修　盧南佑

（指導教授 Advisor）

蔡協燉

系（所、學位學程）主管 Director: 葉嘉陽

摘要

本研究提出一種閉迴路反饋流動控制策略，旨在減緩渦旋引致振動並穩定受流固耦合影響下的剛性圓柱擺動動態。該圓柱可因尾流中渦旋脫落而自由地進行橫向（橫流方向）振盪。數值模擬採用沈浸邊界投影法，結合不可壓縮流的流固耦合數值模型。以靜止圓柱周圍的時間平均流場作為基態，該流場波動微弱，並在圓柱固定座標系中對不可壓縮納維-斯托克斯方程進行線性化。基於該線性系統進行預解分析，構建用於模型參考自適應控制系統的參考模型。研究比較了法向與切向制動兩種作用方式，結果顯示切向制動顯著優於法向制動，分別在升力波動、橫向速度波動與阻力波動方面達到約 85%、84% 與 93% 的減幅。模型參考自適應控制系統框架在適當的自適應學習率範圍內表現出穩定的控制效果，顯示其在有效抑制流固耦合系統中的渦旋引致振動方面的潛力。

關鍵字：渦旋引致振動、流固耦合、流體控制、閉迴路控制、自適應控制

doi:10.6342/NTU202503926

Abstract

This study proposes a closed-loop feedback control strategy to mitigate vortex–induced vibrations and stabilize the plunging dynamics of a rigid circular cylinder undergoing flow–structure interaction (FSI) in a uniform stream. The cylinder is free to oscillate transversely (crossflow) due to vortex shedding in its wake. Numerical simulations are conducted using the immersed boundary projection method, integrating a coupled fluid–structure interaction formulation for incompressible flow. A time–averaged flow field around a stationary cylinder, characterized by minimal fluctuations, serves as the base state to linearize the incompressible Navier–Stokes equations in a cylinder–fixed frame. Resolvent analysis of this linearized system is then employed to derive a reference model for the model reference adaptive control (MRAC) scheme. Both normal and tangential actuation configurations are examined. The results show that tangential actuation significantly outperforms normal actuation, achieving reductions of up to 85% in lift fluctuations, 84% in transverse velocity fluctuations, and 93% in drag fluctuations, all with minimal in-

doi:10.6342/NTU202503926

put power. The MRAC framework demonstrates robust and stable control effectiveness across a suitable range of adaptive learning rates, highlighting its potential for effectively suppressing flow-induced vibrations in fluid–structure interaction systems.

Keywords: Vortex-Induced Vibration, Flow-Structure Interaction, Flow Control, Closed-loop Control, Adaptive Control

doi:10.6342/NTU202503926

Contents

doi:10.6342/NTU202503926

doi:10.6342/NTU202503926

List of Figures

doi:10.6342/NTU202503926

doi:10.6342/NTU202503926

doi:10.6342/NTU202503926

Denotation

$\mathcal{A}$	Discrete time-invariant linear system operator of the reference model $W_m(s)$
$\mathcal{B}$	Forcing matrix in a SISO system
C	Courant–Friedrichs–Lewy (CFL) number, $C = \frac{u_{max}\Delta t}{\Delta x}$
C_D	Drag coefficient, $C_D = \frac{F_x}{\frac{1}{2}\rho_f U_\infty^2 D}$
C_L	Lift coefficient, $C_L = \frac{F_y}{\frac{1}{2}\rho_f U_\infty^2 D}$
$\mathcal{C}$	Sensing matrix in a SISO system
D	Circular cylinder diameter
$\mathcal{D}$	Nonlinear disturbance matrix to the SISO system
F	Total force on the body surface
f_a	Control amplitude generated by adaptive control
$\mathbf{f}$	Nondimensional surface stress from body to fluid

doi:10.6342/NTU202503926

$\mathbf{f}_1$	External forcing
$g(\sigma_g, r, \theta_a)$	2D Gaussian filter
G_p	Plant of actual system
Γ	The first learning rate for the adaptive gains
Γ_b	The interface between the body and flow
γ	The second learning rate for the adaptive gains
$\mathbf{I}$	Identity matrix
L_c	Characteristic length
M_e	Effective mass
p	Pressure field in inertial frame
$P(s)$	The SISO transfer function between the control input to the sensing signal
ρ_b	Dimensionless solid body density
ρ_e	Effective density, $\rho_e = \rho_b/\rho_f - 1$
ρ_f	Dimensionless fluid density
$\mathbf{P}_v$	Projection matrix, projects the force on only the transverse direction
σ_g	The width of 2D Gaussian function $g(\sigma_g, r, \theta_a)$
θ_a	Angle from the stagnation point to actuator position

doi:10.6342/NTU202503926

θ_p	Phase of the cylinder plunging,
$\boldsymbol{\theta}_c$	Adaptive gains vector, $\boldsymbol{\theta}_c^\top = [c_0(t),\, \theta_1^\top(t),\, \theta_2^\top(t),\, \theta_3(t)]$
Re	Reynolds number, $Re = U_\infty D$
$\mathcal{R}_x$	The relative fluctuation reduction quantity for the time-series data x
St_p	Struhal number of cylinder plunging frequency, $St_p = f_p D/U_\infty$
St_{vs}	Struhal number of vortex shedding frequency
U_∞	Uniform free stream velocity
V_b	Cylinder transverse velocity
v'	Flow velocity of sensor position in transverse direction in body-fixed frame
$\chi(s)$	Lagrangian coordinate on the body surface Γ_b
$\mathbf{u}$	Nondimensional flow velocity in the inertial frame
$\mathbf{u}_n$	Nondimensional flow velocity in the non-inertial frame
$\boldsymbol{\omega}_n$	Nondimensional vorticity in the inertial frame
$\boldsymbol{\omega}$	Regressor vector, $\boldsymbol{\omega} = [r,\, \omega_1,\, \omega_2,\, y_p]^\top$
$\boldsymbol{\omega}_n$	Nondimensional vorticity in the non-inertial frame
y_p	Output signal of G_p

doi:10.6342/NTU202503926

Chapter 1 Introduction

1.1 The Challenge of Flow-Induced Vibration

Flow-induced vibration (FIV) arises from the resonant interaction between unsteady fluid flow and flexible or movable structures, often leading to fatigue damage, performance loss, or catastrophic failure. This phenomenon poses significant challenges in various engineering fields, including marine, civil, and aerospace applications [1]. A canonical case for studying FIV is the flow past a circular cylinder, well known for its vortex shedding that induces periodic forcing on the structure. Reviews by Sarpkaya [2] and Williamson and Govardhan [3] classify the wake modes and amplitude responses, providing foundational insight into the complex nonlinear fluid–structure interactions. These works underscore the key role of vortex shedding in sustaining structural oscillations and the persistent challenge of modeling and controlling such nonlinear dynamics to mitigate adverse effects and enhance stability.

1.2 Flow Control Methods

Flow control strategies are commonly categorized as passive or active. Passive control, the earliest class of methods, relies on fixed geometric modifications that require no

doi:10.6342/NTU202503926

external energy input. For example, Gómez-de-Segura and García-Mayoral [4] demonstrated that anisotropic permeable substrates can reduce turbulent drag by altering near-wall flow structures. Similarly, Mao *et al.* [5] showed that flexible hairy coatings attached to bluff bodies reduce drag by stabilizing the wake through shape adaptation and delaying vortex formation. While passive methods offer reliability and simplicity, their fixed geometry limits adaptability under varying flow conditions. Active flow control, on the other hand, employs powered actuators—such as synthetic jets and base blowing or suction—to dynamically reduce flow fluctuations. This adaptability enables improved performance across a wide range of operating conditions and has driven extensive recent research. A comprehensive review of these methods is provided by Chen et al. [1]. For instance, Nair *et al.* [6] developed a sensor-based, energy-efficient phase-control framework that actively manipulates vortex shedding timing in periodic bluff-body flows using phase-reduction analysis and optimal control inputs, enabling rapid and precise modulation of flow oscillations to enhance aerodynamic performance. Furthermore, Maryami and Liu [7] applied steady base blowing to suppress tonal noise and modify wake instabilities.

Modern active control techniques typically use feedback architectures, where sensor measurements inform real-time actuation. These techniques can be broadly categorized as data-driven or model-based control. Data-driven methods, particularly model-free approaches based on reinforcement learning (RL), have gained prominence for discovering control policies without relying on explicit flow models. For example, Rabault et al.[8] demonstrated that deep RL can autonomously learn effective jet-based actuation strategies to stabilize the wake behind a circular cylinder. This flexibility extends to systems with moving boundaries; Jiang and Cao[9] applied RL to control a transversely oscillating cylinder, achieving an 8.4% drag reduction by adjusting the oscillation amplitude in real

doi:10.6342/NTU202503926

time.

Model-based control provides insights into complex, often high-dimensional flow systems by reducing them to low-order approximations known as reduced-order models (ROMs). These ROMs capture the dominant dynamics of the flow and are typically constructed using modal decomposition techniques. Towne et al.[10] demonstrated that Spectral Proper Orthogonal Decomposition (SPOD) is theoretically equivalent to resolvent analysis in the frequency domain and to online Dynamic Mode Decomposition (DMD) in the time domain, offering a unified framework for analyzing input-output behavior in turbulent flows. Adaptive variants such as online DMD have been developed to enable real-time model updates for unsteady and time-varying systems. For example, Deem et al.[11] applied online DMD to track the evolving dynamics of a separated boundary layer and implemented a recursive feedback controller to maintain flow attachment. Similarly, Lin and Tsai [12] combined resolvent-based modeling with adaptive and robust control techniques to stabilize the flow around a periodically forced plunging cylinder, demonstrating the benefits of adaptability in systems with moving boundaries.

1.3 Resolvent Analysis in Flow Control

Resolvent analysis provides a rigorous, physics-based framework for constructing ROMs that are well suited to flow control applications. By linearizing the Navier–Stokes equations around a steady or time-averaged base flow, the resolvent operator characterizes a frequency-dependent input-output relationship between nonlinear forcing and flow response [13]. This approach reveals the dominant amplification mechanisms within the flow, offering key insights into how specific actuation strategies influence coherent flow

doi:10.6342/NTU202503926

structures [10]. For instance, Yeh and Taira [14] utilized classical resolvent analysis to guide open-loop separation control over airfoils, while Leclercq et al. [15] developed iterative feedback controllers to stabilize quasiperiodic cavity flows. To extend this framework to time-periodic base flows, Padovan et al.[16] introduced the harmonic resolvent framework, which captures amplification mechanisms and cross-frequency interactions in nonlinear, time-periodic flows. Building on this, Padovan and Rowley[17] applied the method to subharmonic flow structures such as vortex pairing in jets, demonstrating its ability to capture triadic frequency interactions. These advancements have broadened the applicability of resolvent analysis in flow control design. More recently, Lin et al. [18] extended resolvent analysis to linear time-periodic systems by incorporating Floquet theory, achieving a 25.7% reduction in lift fluctuations for a plunging cylinder.

1.4 Flow Control of Fluid-Structure Interaction Systems

The application of advanced feedback strategies to fluid-structure interaction (FSI) systems has achieved significant success, primarily in the context of elastically mounted or tethered bodies exhibiting vortex-induced vibration (VIV). A landmark example is the work by Yao and Jaiman [19], who used a ROM constructed with the Eigensystem Realization Algorithm (ERA) to design an active blowing and suction controller that successfully stabilized VIV in an elastically mounted cylinder. Following this, Ren et al. [20] introduced a machine-learning-based approach using genetic programming to develop feedback control laws, achieving over 94% suppression of VIV amplitude and robust control performance. McQueen et al. [21] subsequently achieved near-complete suppression of a sphere's vibrations across various response regimes.

doi:10.6342/NTU202503926

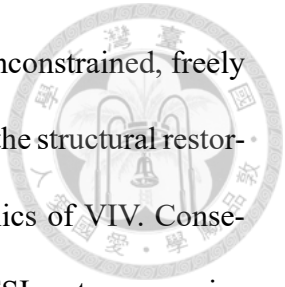

However, a distinct class of FSI problems involves the VIV of unconstrained, freely moving bodies. These systems present unique challenges, as they lack the structural restoring forces and well-defined natural frequencies central to the dynamics of VIV. Consequently, the development of feedback control for such unconstrained FSI systems remains a less-explored area. Furthermore, the inherent time-varying and nonlinear dynamics of these fully coupled systems suggest that an effective control strategy must also be adaptive. This motivates the search for a physically informed, adaptive framework suitable for the unique challenges of unconstrained FSI problems.

1.5 Motivation and Thesis Structure

This study develops a feedback control strategy based on model reference adaptive control (MRAC) for a rigid circular cylinder undergoing free plunging motion induced by flow–structure interaction. The primary goal is to reduce unsteady fluctuations in the flow-structure system, with particular focus on minimizing force fluctuations and suppressing the amplitude of the cylinder's oscillations. To achieve this, we construct an adaptive control framework that guides the system to track a desired reference behavior derived from physical insight. This approach uniquely integrates a model reference adaptive control architecture with a reference model informed by resolvent analysis, and applies it to the vortex-induced motion of an unconstrained body in two-dimensional laminar flow. The paper is structured as follows: §2 presents the problem formulation and control design; §3 details the numerical methods employed; §4 discusses the results and evaluates the control performance; and §5 concludes with a summary and perspectives for future work.

doi:10.6342/NTU202503926

Chapter 2 Problem Setup and Control Method

In this thesis, a canonical FSI system is examined as a representative unsteady flow configuration. The system comprises a rigid circular cylinder immersed in an unbounded, incompressible free stream. The cylinder is constrained from rotating but allowed to translate in the cross-flow direction. Initially at rest, the cylinder begins to oscillate transversely due to alternating vortex shedding in its wake. This vortex-induced motion, driven by the interplay between unsteady fluid forces and structural dynamics, amplifies flow fluctuations and sustains a periodic response. This configuration serves as a fundamental model for investigating FSI behavior.

Flow control techniques have demonstrated strong potential in mitigating unsteady flow phenomena and are therefore considered an effective strategy for managing FSI systems. The main objective of this study is to attenuate the coupled fluctuations in the fluid and structural responses, specifically by reducing the unsteady lift forces acting on the cylinder and minimizing the amplitude of its transverse motion. To accomplish this, it is essential to first gain a comprehensive understanding of the underlying flow physics before formulating and applying an appropriate control strategy.

This chapter presents the problem formulation and control method. Section 2.1 in-

doi:10.6342/NTU202503926

troduces the flow physics and configuration of the FSI system. Section 2.2 formulates the governing equations for the fluid and structure, including flow-structure interaction. Section 2.3 outlines the linearization of the flow equations for resolvent analysis and control design. Finally, Section 2.4 introduces the MRAC strategy and discusses its integration within the overall flow control framework.

2.1 Physical Problem Setup

Consider the flow past a rigid circular cylinder immersed in an incompressible, uniform free stream. The cylinder is fixed against rotation and streamwise translation but is free to move in the transverse (cross-flow) direction. The flow around the cylinder becomes unstable, resulting in the formation of a periodic von Kármán vortex street in its wake.

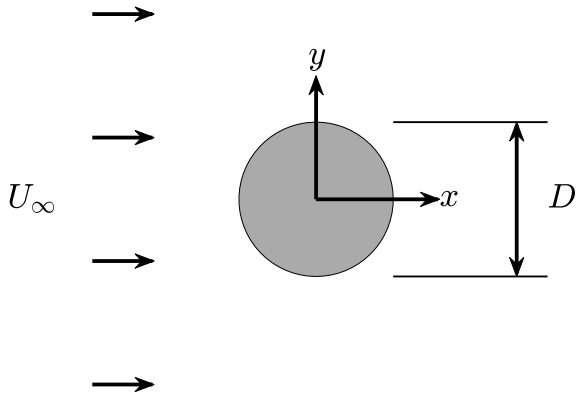

Figure 2.1: Circular cylinder immersed in a uniform flow.

Figure 2.1 demonstrates the configuration of a circular cylinder immersed in a uniform flow, which serves as the canonical setup for investigating vortex-induced motion. The periodic shedding of vortices generates significant unsteady fluid forces on the cylinder, primarily in the transverse direction. The cylinder's transverse motion influences the timing and strength of vortex shedding, creating a coupled feedback loop between the

doi:10.6342/NTU202503926

fluid forces and structural response. This bidirectional interaction leads to resonance-like behavior, causing large-amplitude, self-sustained plunging oscillations. Such dynamics provide a canonical model for VIV, where the structure's response is driven by inertia and flow-induced forcing alone.

The fluid dynamics are governed by the two-dimensional, incompressible Navier–Stokes equations, expressed in nondimensional form within an inertial (laboratory-fixed) reference frame as:

$$\frac{\partial \mathbf{u}}{\partial t} + (\mathbf{u} \cdot \nabla)\mathbf{u} = -\nabla p + \frac{1}{Re}\nabla^2 \mathbf{u}, \tag{2.1}$$

$$\nabla \cdot \mathbf{u} = 0, \tag{2.2}$$

$$\mathbf{u} \to \mathbf{U}_\infty \quad \text{as} \quad |\mathbf{x}| \to \infty, \tag{2.3}$$

where $\mathbf{u}(\mathbf{x}, t)$ denotes the velocity field, and $p(\mathbf{x}, t)$ represents the pressure. The right-hand side of the momentum equation contains the viscous diffusion term, $\frac{1}{Re}\nabla^2 \mathbf{u}$, which accounts for the effect of viscosity in the flow. Here, the Reynolds number $Re = \frac{U_\infty D}{\nu}$ characterizes the ratio of inertial to viscous forces, with ν denoting the kinematic viscosity of the fluid. The continuity equation (2.2) enforces the incompressibility condition, ensuring that the volume of any fluid element remains constant over time. The far-field condition (2.3) specifies that the velocity approaches the uniform free-stream velocity $\mathbf{U}_\infty$ at large distances from the body.

The presence of the cylinder introduces a moving solid boundary within the fluid domain. The interaction between the flow and the solid structure occurs through surface stresses, which include both pressure and viscous contributions acting along the cylinder's surface. These forces determine the motion of the cylinder in the transverse direction

doi:10.6342/NTU202503926

and form the core of the FSI.

The transverse dynamics of the cylinder are described by Newton's second law:

$$M\ddot{y}(t) = F_y(t), \tag{2.4}$$

where M is the mass per unit length of the cylinder, and $\ddot{y}(t)$ is its transverse acceleration. The net force $F_y(t)$ results from the integration of pressure and viscous shear stresses over the surface of the cylinder, obtained from the fluid solution.

To quantify the flow-induced forces, the fluid force is decomposed into two orthogonal components: the drag force $F_x(t)$ in the streamwise direction and the lift force $F_y(t)$ in the transverse direction. These are nondimensionalized as follows:

$$C_D(t) = \frac{F_x(t)}{\frac{1}{2}\rho_f U_\infty^2 D}, \qquad C_L(t) = \frac{F_y(t)}{\frac{1}{2}\rho_f U_\infty^2 D}, \tag{2.5}$$

where ρ_f is the fluid density. The lift and drag coefficients, C_L and C_D , provide standardized metrics for evaluating the unsteady forces acting on the cylinder and are critical indicators of VIV behavior.

2.2 Immersed Boundary Formulation for Flow-Structure Interaction

To model the FSI of a rigid body immersed in an incompressible, uniform free stream, we adopt an immersed boundary projection method (IBPM). The formulation is based on the target-fixed framework of Lin et al. [22], which extends the projection method of Taira & Colonius [23] to solve FSI problems efficiently and non-iteratively. In this approach,

doi:10.6342/NTU202503926

the governing equations are solved in a non-inertial reference frame that is attached to the body, whose surface is denoted by Γ_b.

Within this body-fixed frame, the fluid is described using Eulerian coordinates ($\mathbf{x}$), while the stationary body surface is represented by time-invariant Lagrangian coordinates ($\boldsymbol{\chi}(s)$). A key advantage of this setup is that it allows surface forces to be applied at fixed locations relative to the grid, thereby obviating the need for iterative interface tracking and enhancing numerical stability.

The dimensionless governing equations are:

$$\frac{\partial \mathbf{u}}{\partial t} = -\nabla \Pi + \mathbf{X}(\mathbf{u} - \mathbf{u}_b)\boldsymbol{\omega} + \frac{1}{Re}\nabla^2 \mathbf{u} + \int_{\Gamma_b} \mathbf{f}(\chi(s), t)\delta(\chi(s) - \mathbf{x})\, \mathrm{d}s, \tag{2.6}$$

$$\nabla \cdot \mathbf{u} = 0, \tag{2.7}$$

$$\int_{\Omega} \mathbf{u}(\mathbf{x}, t)\delta(\mathbf{x} - \chi(s))\, \mathrm{d}\mathbf{x} = \mathbf{u}_b(t), \tag{2.8}$$

$$M_e \frac{\mathrm{d}\mathbf{u}_b}{\mathrm{d}t} = -\int_{\Gamma_b} \mathbf{P}_v \mathbf{f}(\chi(s), t)\, \mathrm{d}s, \tag{2.9}$$

with the following definitions:

$$\Pi = p + \frac{1}{2}|\mathbf{u} - \mathbf{u}_b|^2, \tag{2.10}$$

$$\rho_e = \rho_b - \rho_f, \tag{2.11}$$

$$M_e = M_b - V_s. \tag{2.12}$$

The governing equations are nondimensionalized using a characteristic length scale L_c and a reference velocity U_∞. The coordinates χ and χ_1 are scaled by L_c, while the velocities $\mathbf{u}$ and $\mathbf{u}_b$ are scaled by U_∞. The gradient operator ∇, volume V_s, and time t are scaled by $1/L_c$, L_c^3, and L_c/U_∞, respectively. The vorticity $\boldsymbol{\omega}$ is scaled by U_∞/L_c, and

doi:10.6342/NTU202503926

both the pressure p and surface force $\mathbf{f}$ are scaled by $\rho_f U_\infty^2$.

All vector quantities in equations (2.6)–(2.12) are defined in the body-fixed frame. The flow velocity $\mathbf{u}$ and vorticity $\boldsymbol{\omega}$ are nondimensional and described in the inertial frame, while $\mathbf{f}$ denotes the nondimensional surface stress exerted by the body on the fluid. The modified pressure Π, defined in (2.10), combines the static pressure and the kinetic energy associated with the relative motion between the fluid and the body. Equation (2.7) enforces the incompressibility condition, and equation (2.8) imposes the no-slip condition on the body surface. Since the cylinder is constrained from rotating, only translational motion is considered. The translational dynamics are governed by equation (2.9), in which the operator $\mathbf{P}_v$ projects the surface stress $\mathbf{f}$ onto the cross-flow direction. This projection accounts for the fact that the body is restricted to move only in the cross-flow direction.

As the Lagrangian points representing the rigid body are projected onto the Eulerian fluid grid, the motion of the fluid enclosed within the body must be accounted for to maintain physical consistency. In this context, the effective density is defined as $\rho_e = \rho_b/\rho_f - 1$, where ρ_b and ρ_f are the nondimensional densities of the body and fluid, respectively. The effective mass M_e, as defined in equation (2.12), incorporates this density difference and represents the net mass contribution of the body relative to the surrounding fluid.

2.3 Linearized Flow System

For model-based control design, it is essential to derive a linear time-invariant (LTI) approximation of the underlying nonlinear FSI dynamics. In this study, we construct such a linear model through resolvent analysis, which characterizes the system dynamics from an input–output perspective and identifies frequency-dependent amplification behaviors.

doi:10.6342/NTU202503926

The resulting LTI system provides a physically interpretable and analytically tractable representation of the flow response, serving as the reference model for the MRAC strategy presented in the following section. The steady base flow of a stationary cylinder, characterized by minimal inherent fluctuations [18], is selected as the reference state for linearization. This time-averaged flow provides a stable and physically meaningful foundation for control-oriented modeling and enables the formulation of a linear operator.

The vorticity equation in the non-inertial, body-fixed frame is derived from the governing equations and forms the foundation for linearization. Incorporating the effects of external forcing, it is expressed as

$$\frac{\partial \boldsymbol{\omega}_n}{\partial t} = \nabla \times [(\mathbf{u}_n - \mathbf{u}_b) \times \boldsymbol{\omega}_n] - \frac{1}{Re} \nabla \times (\nabla \times \boldsymbol{\omega}_n) + \nabla \times \mathbf{f}_1, \tag{2.13}$$

where $\boldsymbol{\omega}_n$ and $\mathbf{u}_n$ are the vorticity and velocity in the non-inertial (body-fixed) frame, $\mathbf{u}_b$ is the velocity of the body (which vanishes in the stationary base case), and $\mathbf{f}_1$ denotes external forcing, which includes both actuation and FSI contributions.

To isolate the dynamics of fluctuations, Reynolds decomposition is applied to the velocity and vorticity fields:

$$\boldsymbol{\omega}_n = \overline{\boldsymbol{\omega}}_n + \boldsymbol{\omega}'_n, \tag{2.14}$$

$$\mathbf{u}_n = \overline{\mathbf{u}}_n + \mathbf{u}'_n, \tag{2.15}$$

where $\overline{\boldsymbol{\omega}}_n$ and $\overline{\mathbf{u}}_n$ are the time-averaged vorticity and velocity fields, respectively, and $\boldsymbol{\omega}'_n$ and $\mathbf{u}'_n$ represent the fluctuating terms.

Substituting these decompositions into the governing equation and retaining only

doi:10.6342/NTU202503926

terms linear in the fluctuations yields the linearized vorticity equation:

$$\frac{\partial \boldsymbol{\omega}'_n}{\partial t} = \underbrace{\nabla \times (\overline{\mathbf{u}}_n \times \boldsymbol{\omega}'_n + \mathbf{u}'_n \times \overline{\boldsymbol{\omega}}_n) - \frac{1}{Re}\nabla \times (\nabla \times \boldsymbol{\omega}'_n)}_{\mathcal{L}_{\boldsymbol{\omega}'_n}}$$

$$+ \underbrace{\nabla \times [\overline{\mathbf{u}}_n \times \overline{\boldsymbol{\omega}}_n + \mathbf{u}'_n \times \boldsymbol{\omega}'_n] - \frac{1}{Re}\nabla \times (\nabla \times \overline{\boldsymbol{\omega}}_n) + \nabla \times \mathbf{f}_1}_{\mathbf{F}}, \quad (2.16)$$

where $\mathcal{L}_{\boldsymbol{\omega}'_n}$ denotes the linear operator governing the perturbation dynamics and $\mathbf{F}$ collects the nonlinear residuals and external forcing.

Following spatial discretization, the system takes the form

$$\frac{\mathrm{d}\mathbf{x}}{\mathrm{d}t} = \mathcal{A}\mathbf{x} + \mathbf{F}, \quad (2.17)$$

where $\mathbf{x}$ is the discrete state vector corresponding to $\boldsymbol{\omega}'_n$, and $\mathcal{A}$ is the discrete linear operator.

To analyze the system's frequency response, we assume harmonic forcing and response:

$$\mathbf{x}(t) = \hat{\mathbf{x}}e^{-i\omega t}, \quad \mathbf{F}(t) = \hat{\mathbf{F}}e^{-i\omega t}, \quad (2.18)$$

yielding the frequency-domain relationship:

$$(-i\omega\mathbf{I} - \mathcal{A})\hat{\mathbf{x}} = \hat{\mathbf{F}}. \quad (2.19)$$

Solving for the response gives

$$\hat{\mathbf{x}} = (-i\omega\mathbf{I} - \mathcal{A})^{-1}\hat{\mathbf{F}}, \quad (2.20)$$

doi:10.6342/NTU202503926

where

$$\mathcal{H}(\omega) = (-i\omega\mathbf{I} - \mathcal{A})^{-1} \tag{2.21}$$

is the resolvent operator. This operator describes the input–output behavior of the linearized system and quantifies how external disturbances are filtered and amplified across frequencies.

The resolvent operator constructed from the stationary base flow provides a reduced-order, physically interpretable representation of the dominant input–output modes of the system. It serves as the foundation for defining a stable reference model used in the MRAC method.

2.4 Model Reference Adaptive Control

Model Reference Adaptive Control is a control method in which adaptive laws continuously adjust controller parameters to achieve the desired system performance. It is based on the principles of Model Reference Control (MRC), where a LTI system, referred to as the reference model, is prescribed to produce the desired output y_m in response to a reference input r. The output of this model defines the target trajectory that the plant output should follow. The overall structure of the reference model and plant is illustrated in Figure 2.2, following the classical MRAC formulation by Ioannou and Sun [24].

If the plant G_p were fully known, the control problem would reduce to a model-matching problem. However, in practical scenarios, the plant dynamics are often unknown or only partially available. For instance, the available information may be limited to the relative degree of the system or the sign of its high-frequency gain.

doi:10.6342/NTU202503926

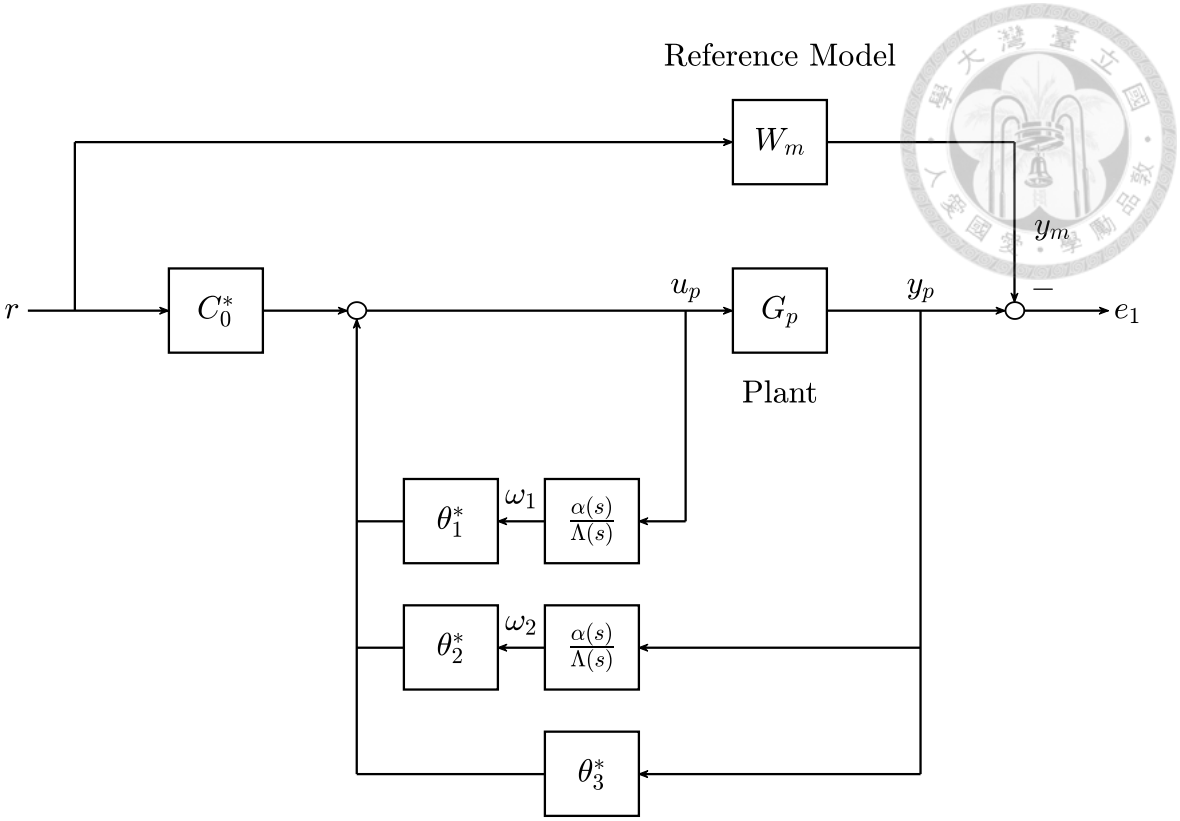

Figure 2.2: Schematic of the MRAC structure showing the reference model and the plant.

In this study, the plant G_p is treated as unknown, and the adaptive controller is designed to minimize the tracking error $e_1 = y_p - y_m$, where y_p is the plant output and y_m is the output of the reference model. The reference model is constructed using resolvent analysis based on the linearized base flow of a stationary cylinder, which characterizes the desired system response. The primary control objective is to reduce fluctuations in the FSI system, including both the lift force and the transverse velocity of the cylinder, by ensuring that the plant output closely follows the reference model output.

A direct adaptive control approach is employed, in which the controller parameters are updated through adaptive laws without requiring explicit identification of the plant dynamics. The control input is defined as

$$u_p = c_0(t)r + \theta_1^\top(t)\omega_1 + \theta_2^\top(t)\omega_2 + \theta_3(t)y_p \equiv \boldsymbol{\theta}_c^\top \boldsymbol{\omega}, \tag{2.22}$$

doi:10.6342/NTU202503926

where u_p is the control input, $\boldsymbol{\theta}_c^\top = [c_0(t),\, \theta_1^\top(t),\, \theta_2^\top(t),\, \theta_3(t)]$ is the adaptive gain vector, and $\boldsymbol{\omega} = [r,\, \omega_1,\, \omega_2,\, y_p]^\top$ is the regressor signal vector. The gains $c_0(t)$, $\theta_1(t)$, $\theta_2(t)$, and $\theta_3(t)$ correspond to feedback gains for the reference input, filtered control input, filtered plant output, and unfiltered plant output, respectively.

The filtered signals $\omega_1(t)$ and $\omega_2(t)$ are obtained by passing $u_p(t)$ and $y_p(t)$ through a stable linear filter of the form $\frac{\alpha(s)}{\Lambda(s)}$, where $\Lambda(s)$ is a monic Hurwitz polynomial. In this study, the filter is chosen as $\frac{1}{s+1}$ for simplicity. These filtered signals satisfy the following state-space realizations:

$$\dot{\omega}_1 = F\omega_1 + gu_p, \tag{2.23}$$

$$\dot{\omega}_2 = F\omega_2 + gy_p, \tag{2.24}$$

where (F, g) is the state-space realization of the selected filter.

The controller parameters are updated using a normalized gradient method that minimizes a cost function J, following the MRAC framework proposed by Ioannou and Sun [24]. The cost function penalizes the discrepancy between the actual and estimated tracking errors and is scaled by a normalization factor to ensure robust adaptation:

$$J(\rho, \boldsymbol{\theta}_c) = \frac{(e_1 - \hat{e}_1)^2}{2m_s^2}, \tag{2.25}$$

where $e_1 = y_p - y_m$ is the tracking error, and $\hat{e}_1$ is the estimated error generated by an internal model.

doi:10.6342/NTU202503926

The intermediate variables are defined as

$$\phi = -W_m(s)\boldsymbol{\omega}, \tag{2.26}$$

$$m_s^2 = 1 + \phi^\top \phi + (W_m(s)u_p)^2, \tag{2.27}$$

$$\hat{e}_1 = \rho \left(\boldsymbol{\theta}_c^\top \phi + W_m(s)u_p \right), \tag{2.28}$$

where $W_m(s)$ is the transfer function of the reference model. The normalization term m_s^2 bounds the adaptive update and improves robustness in real-time operation, particularly when the regressor signal becomes large [24].

Applying the gradient descent method to minimize J, the normalized adaptive laws are derived as

$$\dot{\boldsymbol{\theta}}_c = -\Gamma \nabla_{\boldsymbol{\theta}_c} J = \Gamma \epsilon \phi \, \mathrm{sgn}(\rho), \tag{2.29}$$

$$\dot{\rho} = -\gamma \nabla_\rho J = \gamma \epsilon \left(\boldsymbol{\theta}_c^\top \phi + W_m(s)u_p \right), \tag{2.30}$$

$$\epsilon = \frac{e_1 - \hat{e}_1}{m_s^2}, \tag{2.31}$$

where Γ and γ are positive constants that determine the update rates of $\boldsymbol{\theta}_c$ and ρ, respectively.

To regulate the adaptation rate, the gradient $\nabla_{\boldsymbol{\theta}_c} J$ is pre-multiplied by a positive-definite matrix. In this study, no preferential weighting is assigned to the elements of $\boldsymbol{\theta}_c$, and a uniform scaling matrix $\Gamma \mathbf{I}$ is used, where Γ is a positive scalar and $\mathbf{I}$ is the identity matrix. Similarly, the update law for ρ is scaled by a positive scalar γ.

The parameters Γ and γ must be carefully chosen to balance convergence speed and stability. They can be tuned through numerical experiments or optimization procedures

doi:10.6342/NTU202503926

to improve control performance and are typically selected as positive scalars or diagonal matrices before the adaptive process begins. In summary, the normalized adaptive laws provide a systematic approach for real-time adjustment of the controller parameters, guiding the plant output to closely follow the desired response defined by the reference model. This direct adaptive control framework aims to minimize the difference between the actual system behavior and the reference model.

doi:10.6342/NTU202503926

Chapter 3 Numerical and Flow Control Setup

In this chapter, the numerical methods, simulation setup, and flow control configurations are introduced in detail. First, the numerical approach for simulating FSI is presented, covering the spatial and temporal discretization schemes, the treatment of flow–structure coupling, and the overall solution procedure in Section 3.1. The numerical setup for the simulations, including the computational domain, boundary conditions, and parameter choices, is then described in Section 3.2. Finally, the setup for implementing the flow control method is discussed in Section 3.3, with attention to actuator setting and the specific control configurations adopted in this study.

3.1 Numerical Method for Flow Structure Interaction

3.1.1 Spatial Discretization and Stress Filtering

Following Section 2.2, the fluid domain is discretized in space to numerically solve the governing equations, and a stress filtering technique is applied to ensure numerical stability and accuracy. The method proposed by Taira and Colonius [23] is adopted to discretize the fluid equations on a two-dimensional, unbounded, uniform staggered Carte-

doi:10.6342/NTU202503926

sian grid. The immersed boundary is represented by a uniformly spaced set of Lagrangian points. All spatial intervals are chosen to be equal, so that $\Delta x = \Delta y = \Delta s$, where Δx and Δy denote the grid spacings in the streamwise and transverse directions, respectively, and Δs represents the spacing between neighboring Lagrangian points along the boundary Γ.

For matrix-based formulations, the cross product between two vectors can be conveniently represented using a skew-symmetric matrix:

$$\mathbf{a} \times \mathbf{b} = \mathbf{X}(\mathbf{a})\mathbf{b} = \mathbf{X}^{\top}(\mathbf{b})\mathbf{a}, \tag{3.1}$$

where $\mathbf{a} = (a_1, a_2, a_3)^{\top}$. The skew-symmetric matrix $\mathbf{X}(\mathbf{a})$ is defined as:

$$\mathbf{X}(\mathbf{a}) = \begin{bmatrix} 0 & -a_3 & a_2 \\ a_3 & 0 & -a_1 \\ -a_2 & a_1 & 0 \end{bmatrix}. \tag{3.2}$$

Since the free-stream velocity U_∞ is uniform along the streamwise direction, the corresponding body translation in this direction is fixed. Therefore, only the cylinder's transverse motion is considered. To enforce this simplification, the projection matrix $\mathbf{P}_v$ is defined to extract the vertical component of the body velocity within the modified framework:

$$\mathbf{P}_v = \begin{bmatrix} 0 & 0 & 0 \\ 0 & 1 & 0 \\ 0 & 0 & 0 \end{bmatrix}. \tag{3.3}$$

doi:10.6342/NTU202503926

The discretized rigid-body equation of motion is expressed as:

$$M_e \frac{d\mathbf{u}_b}{dt} = \mathbf{P}_v \mathbf{S} \mathbf{W} f_b, \tag{3.4}$$

where f_b denotes the discretized surface stress on the immersed boundary, obtained from the continuous form $-\mathbf{f}(\chi(s), t)$. A straightforward discretization of the surface stress can introduce spurious oscillations and numerical instability [22]. To mitigate this issue, a stress filter $\mathbf{W}$, proposed by Goza et al. [25], is applied to ensure a physically consistent and numerically stable representation. The resulting filtered stress $\mathbf{W} f_b$ corresponds to the following continuous expression:

$$\frac{\displaystyle\int_\Omega \int_\Gamma \left(-\mathbf{f}(\chi(s))\right) \delta(\chi(s) - \mathbf{x}) \delta(\mathbf{x} - \chi(s))\, ds\, d\mathbf{x}}{\displaystyle\int_\Gamma \delta(\mathbf{x} - \chi(s))\, ds}. \tag{3.5}$$

The numerical delta function used here follows the formulation by Roma [26]:

$$d(r) = \begin{cases} \frac{1}{6\Delta r}\left[5 - 3\frac{|r|}{\Delta r} - \sqrt{-3\left(1 - \frac{|r|}{\Delta r}\right)^2 + 1}\right], & \text{for } 0.5\Delta r \le |r| \le 1.5\Delta r, \\ \frac{1}{3\Delta r}\left[1 + \sqrt{-3\left(\frac{r}{\Delta r}\right)^2 + 1}\right], & \text{for } |r| \le 0.5\Delta r, \\ 0, & \text{otherwise}, \end{cases} \tag{3.6}$$

where $|r|$ is the distance from a Lagrangian point to the center of a nearby grid cell, and Δr is the grid spacing.

The matrix $\mathbf{W}$ is diagonal and symmetric, satisfying $\mathbf{W}^\top = \mathbf{W}$. The linear operator $\mathbf{S}$ discretizes the integral $\int_\Gamma (\cdot)\, ds$. Defining $\mathbf{M} = \mathrm{diag}(M_e \mathbf{I}_3)$, where $\mathbf{I}_3$ is the 3×3 identity

doi:10.6342/NTU202503926

matrix, $\lambda = \mathbf{u}_b$, and $\mathbf{Q} = \mathbf{P}_v\mathbf{S}\mathbf{W}$, equation (3.4) becomes:

$$\mathbf{M}\frac{d\lambda}{dt} = \mathbf{Q}f_b. \tag{3.7}$$

The discretized fluid equations are written as:

$$\frac{dq}{dt} = -\mathbf{G}\Pi + \mathbf{N}(q, q_b) + \frac{1}{Re}\mathbf{L}q - \mathbf{H}f_b, \tag{3.8}$$

$$\mathbf{D}q = 0, \tag{3.9}$$

$$\mathbf{E}q = \mathbf{W}^\top\mathbf{S}^\top\mathbf{u}_b = \mathbf{Q}^\top\lambda + (1 - \mathbf{Q}^\top)\lambda, \tag{3.10}$$

where q and Π are the discretized velocity flux and pressure. The operators $\mathbf{G}$, $\mathbf{D}$, and $\mathbf{L}$ represent the discrete gradient, divergence, and Laplacian, respectively. The nonlinear convection operator $\mathbf{N}(q, q_b)$ approximates $\mathbf{X}(\mathbf{u} - \mathbf{u}_b)\boldsymbol{\omega}$. The regularization and interpolation operators $\mathbf{H}$ and $\mathbf{E}$ correspond to integrals over the immersed boundary Γ. For efficiency, these operators satisfy $\mathbf{D} = -\mathbf{G}^\top$ and $\mathbf{H} = \mathbf{E}^\top$. The appearance of $\mathbf{Q}^\top$ in (3.10) is convenient for later use in control-related formulations.

Following Colonius and Taira [23], the discrete curl operator $\mathbf{C}$ is introduced such that it lies in the null space of the divergence operator $\mathbf{D}$ and satisfies the vector identities $\nabla\cdot(\nabla\times\mathbf{v}) = 0$ and $\nabla\times(\nabla\phi) = 0$. This construction ensures that $\mathbf{D}\mathbf{C} = -(\mathbf{C}^\top\mathbf{G})^\top = 0$. By setting $q = \mathbf{C}s$ and applying $\mathbf{C}^\top$ to equation (3.8), the incompressibility condition (3.9) is automatically satisfied, and the pressure gradient term is eliminated. As a result, the governing equation becomes:

doi:10.6342/NTU202503926

$$\mathbf{C}^\top \mathbf{C} \frac{ds}{dt} = \mathbf{C}^\top \mathbf{N}(q, q_b) + \frac{1}{Re} \mathbf{C}^\top \mathbf{L} \mathbf{C} s - \mathbf{C}^\top \mathbf{E}^\top f_b, \tag{3.11}$$

$$\mathbf{E}\mathbf{C} s = \mathbf{Q}^\top \lambda + (1 - \mathbf{Q}^\top)\lambda. \tag{3.12}$$

3.1.2 Temporal Discretization

At each time step, the governing equations (3.4) and (3.11) are integrated over the interval $[t_n, t_{n+1}]$. The nonlinear convective terms are advanced using the second-order Adams–Bashforth scheme, while the diffusive terms in (3.11) are treated implicitly via the Crank–Nicolson method. Since the operators **E** and **W** are defined in the body-fixed frame and both $\mathbf{C}^\top$ and **S** remain constant in time, the forcing terms $\mathbf{Q} f_b$ and $-\mathbf{C}^\top \mathbf{E}^\top f_b$ can be evaluated outside the temporal integration.

Accordingly, the average immersed-boundary surface stress over the time interval is defined as $\bar{f}_b^{n+1} \equiv \frac{1}{\Delta t} \int_{t_n}^{t_{n+1}} f_b \, dt$, allowing us to solve directly for $\bar{f}_b^{n+1} \Delta t$ in equations (3.4) and (3.11). This treatment enables exact integration of the FSI force terms without additional assumptions in body-fixed frame. The no-slip condition (3.12) is evaluated explicitly at t_{n+1} and expressed in a form convenient for the subsequent derivation.

The semi-discrete equations provides the following symmetric, fully discrete linear system:

$$\begin{pmatrix} \mathbf{C}^\top \mathbf{A} \mathbf{C} & 0 & \mathbf{C}^\top \mathbf{E}^\top \\ 0 & \mathbf{M} & -\mathbf{Q} \\ \mathbf{E}\mathbf{C} & -\mathbf{Q}^\top & 0 \end{pmatrix} \begin{pmatrix} s^{n+1} \\ \lambda^{n+1} \\ \bar{f}_b^{n+1} \Delta t \end{pmatrix} = \begin{pmatrix} r_1^n \\ r_2^n \\ r_3^{n+1} \end{pmatrix}, \tag{3.13}$$

doi:10.6342/NTU202503926

where

$$\mathbf{A} = \mathbf{I} - \frac{\Delta t}{2Re}\mathbf{L}, \tag{3.14}$$

$$r_1^n = \mathbf{C}^\top \left(\mathbf{I} + \frac{\Delta t}{2Re}\mathbf{L}\right)\mathbf{C}s^n + \frac{3\Delta t}{2}\mathbf{C}^\top \mathbf{N}(q^n, q_b^n) - \frac{\Delta t}{2}\mathbf{C}^\top \mathbf{N}(q^{n-1}, q_b^{n-1}), \tag{3.15}$$

$$r_2^n = \mathbf{M}\lambda^n, \tag{3.16}$$

$$r_3^{n+1} = (1 - \mathbf{Q}^\top)\lambda^{n+1}. \tag{3.17}$$

The simplicity of the system (3.13) hinges on the assumptions of rigid-body dynamics formulated in the body-fixed frame and the consideration of a single FSI body.

To solve the system efficiently, a block-LU decomposition is applied, leading to the following sequential steps:

$$\begin{pmatrix} \mathbf{C}^\top\mathbf{A}\mathbf{C} & 0 \\ 0 & \mathbf{M} \end{pmatrix} \begin{pmatrix} s^* \\ \lambda^* \end{pmatrix} = \begin{pmatrix} r_1^n \\ r_2^n \end{pmatrix}, \tag{3.18}$$

$$(\mathbf{Q}^\top\mathbf{M}^{-1}\mathbf{Q} + \mathbf{E}\mathbf{C}(\mathbf{C}^\top\mathbf{A}\mathbf{C})^{-1}\mathbf{C}^\top\mathbf{E}^\top)\bar{f}_b^{n+1}\Delta t = \mathbf{E}\mathbf{C}s^* - \mathbf{Q}^\top\lambda^* - r_3^{n+1}, \tag{3.19}$$

$$\begin{pmatrix} s^{n+1} \\ \lambda^{n+1} \end{pmatrix} = \begin{pmatrix} s^* \\ \lambda^* \end{pmatrix} + \begin{pmatrix} -(\mathbf{C}^\top\mathbf{A}\mathbf{C})^{-1}\mathbf{C}^\top\mathbf{E}^\top\bar{f}_b^{n+1}\Delta t \\ \mathbf{M}^{-1}\mathbf{Q}\,\bar{f}_b^{n+1}\Delta t \end{pmatrix}. \tag{3.20}$$

The factorized steps (3.18)–(3.20) form a fractional-step procedure based on a body-fixed formulation with filtered surface stress and time-averaged FSI forces. Physically, the trial streamfunction and rigid-body velocity are first obtained by advancing the system without enforcing the no-slip condition. The Poisson-like system (3.19) is then solved to compute the immersed boundary stress required to satisfy this constraint. Finally, the trial solutions are projected to enforce the no-slip condition.

doi:10.6342/NTU202503926

To solve the trial streamfunction in (3.18), a multi-domain setup is employed to accurately impose far-field boundary conditions. The Poisson-like operator $(\mathbf{C}^\top \mathbf{A}\mathbf{C})^{-1}$ is inverted efficiently using discrete sine transforms, and the symmetric, time-invariant system in (3.19) is precomputed and solved using Cholesky decomposition.

3.2 Numerical Setup

Consider a rigid circular cylinder immersed in an unbounded, incompressible free stream, subject to flow–structure interaction (FSI). The flow is characterized by a low Reynolds number set to 100, remaining laminar and approximately quasi-two-dimensional. The cylinder's motion is analyzed in a body-fixed coordinate system, with the transverse velocity denoted by V_b. The primary observation domain extends $6D$ in the streamwise direction and $3D$ in the crossflow direction, with the cylinder centered vertically and positioned $1D$ downstream of the inlet. The actuator forces applied near the cylinder surface are represented by red arrows and denoted as f_a, while v' represents the transverse velocity signal of the flow. Both f_a and v' will be detailed in subsequent sections. This domain serves as the observation region for analyzing the FSI system and conducting the resolvent analysis described in Section 2.3, as illustrated in Figure 3.2. A multi-domain approach is adopted to balance accurate far-field boundary conditions with computational efficiency. An example configuration of this setup is shown in Figure 3.1.

To simulate this FSI system, the immersed boundary projection method (IBPM), extended from Lin et al. [22], is employed. The surface of the cylinder is discretized using uniformly spaced Lagrangian points, which are projected onto a fluid grid fixed in the body-fixed frame to enforce the no-slip condition at the fluid–structure interface. To en-

doi:10.6342/NTU202503926

sure spatial consistency between the immersed boundary and the fluid grid, the spacing is uniformly set such that $\Delta s = \Delta x = \Delta y = 0.03D$. Following Lin et al. [22], the grid Reynolds number, defined as $Re_g = U_\infty \Delta x/\nu$, is maintained below 5, which has been shown to yield a spatial convergence rate of approximately 1.5. The time step Δt is chosen to keep the Courant-Friedrichs-Lewy (CFL) number, $C = \frac{u_{\max}\Delta t}{\Delta x}$, below 0.04 for numerical stability, and is set to $\Delta t = 0.001$ in this study.

The computational domain is designed using a six-level nested multi-domain configuration to accurately enforce far-field boundary conditions while ensuring computational efficiency. The innermost domain, which has the finest grid, extends $6D$ in the streamwise direction and $3D$ in the transverse direction. The cylinder is placed $1D$ downstream from the inlet and $1.5D$ above the lower boundary within this finest region. This area captures the key near-wake dynamics and also serves as the observation region for the resolvent analysis.

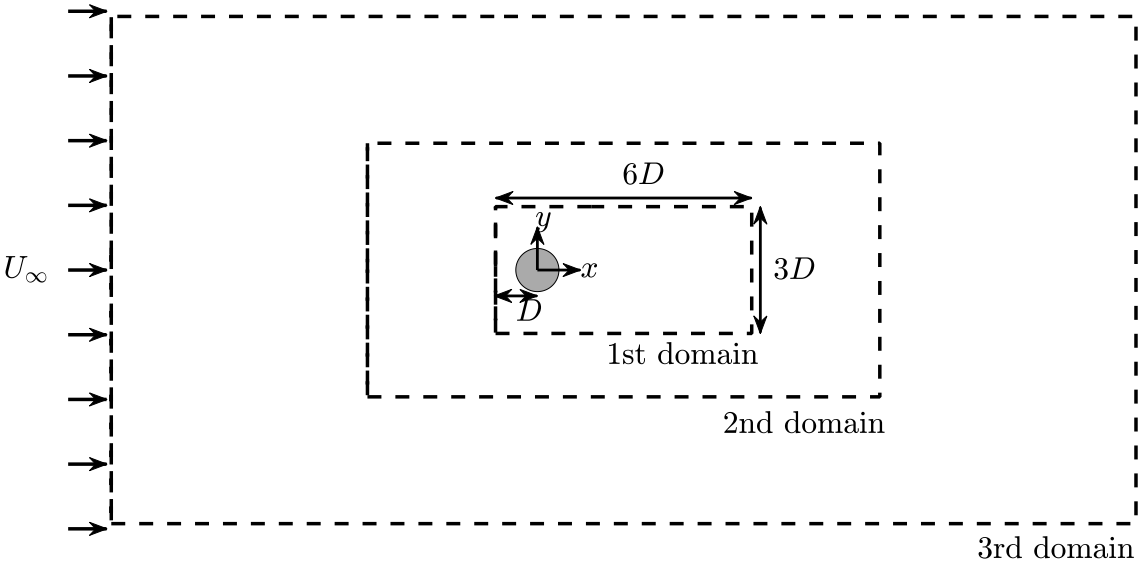

Figure 3.1: Example of a 3-level multi-domain configuration.

Each surrounding domain is twice as large and has double the grid spacing compared to the inner one, creating a hierarchical mesh that becomes progressively coarser toward

doi:10.6342/NTU202503926

the far field. This approach provides sufficient spatial resolution near the cylinder—where unsteady flow features and vortex generation occur—while reducing computational cost in less critical regions. A uniform free-stream velocity U_∞ is applied at the boundary of the largest domain to ensure inflow conditions.

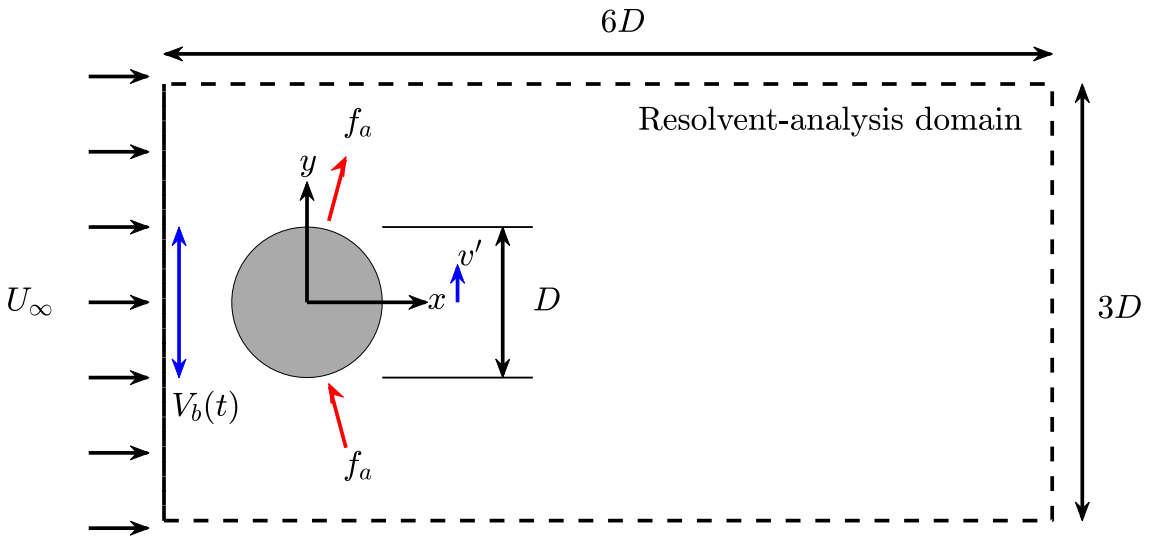

(a) Normal actuation

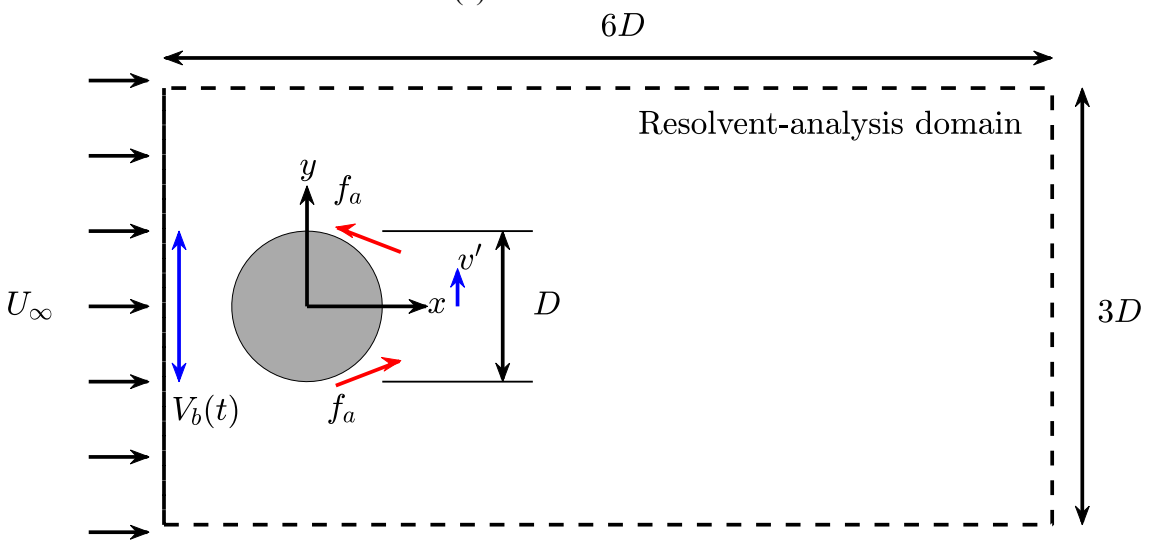

(b) Tangential actuation

Figure 3.2: Observation domain of control flow system. This domain is used for resolvent analysis with the finest grid. (a) Normal and (b) tangential actuation at the same position.

doi:10.6342/NTU202503926

3.3 Flow Control Setup

This section describes the formulation of a control-oriented flow system designed to suppress the plunging motion of a rigid circular cylinder induced by FSI. The objective is to develop a clear input–output representation of the fluid system, enabling the application of active feedback control.

To implement active flow control, a pair of body forces, denoted by f_a, is applied to the fluid near the surface of the cylinder, mimicking the use of a dielectric barrier discharge (DBD) actuator to force the fluid [14]. These forces are placed symmetrically above and below the cylinder at polar coordinates $(r, \theta_a) = (0.6D, 110°)$, measured from the cylinder center. The direction of actuation is categorized as either normal or tangential to the cylinder surface, as shown in 3.2. For normal actuation, a pair of antisymmetric forces is applied at the top and bottom of the cylinder, simulating the effect of zero-net-mass-flux actuators. For tangential actuation, a pair of antisymmetric forces is applied along the surface of the cylinder.

The actuators are mathematically represented as:

$$\mathbf{f}(x, y) = B(x, y)\, f_a, \tag{3.21}$$

$$B(x, y) = \begin{bmatrix} \cos\left(g(\sigma_g, r, \theta_a) - g(\sigma_g, r, -\theta_a)\right) \\ \sin\left(g(\sigma_g, r, \theta_a) + g(\sigma_g, r, -\theta_a)\right) \end{bmatrix}, \tag{3.22}$$

where r is the radial distance from the center of the cylinder, and the two-dimensional Gaussian function $g(\sigma_g, r, \theta_a)$ determines the location and spread of the actuator force:

doi:10.6342/NTU202503926

$$g(\sigma_g, r, \theta_a) = \frac{1}{2\pi\sigma_g^2} \exp\left(-\frac{(x - r\cos\theta_a)^2 + (y - r\sin\theta_a)^2}{2\sigma_g^2}\right), \tag{3.23}$$

with σ_g specifying the spatial spread of the forcing region. To provide a quantitative measure of the control effort, the power coefficient C_P is introduced. This coefficient quantifies the input power required by the model reference adaptive control and is defined as:

$$C_P = \frac{\int f_a u_{jet}}{\frac{1}{2}\rho_f U_\infty^2 D}, \tag{3.24}$$

Next, the spatially discretized vorticity equation described in (2.17) is expressed in a state-space form suitable for control analysis:

$$\frac{d\mathbf{x}}{dt} = \mathcal{A}\mathbf{x} + \mathcal{B}u + \mathcal{D}, \tag{3.25}$$

where $\mathbf{x}$ is the discretized fluctuation state (e.g., vorticity), $\mathcal{A}$ is the time-invariant linear system operator, $\mathcal{B}$ maps the control input u to the flow domain, and $\mathcal{D}$ represents the nonlinear disturbance, including contributions from flow–structure interaction.

To obtain a measurable output for feedback, a sensing operator $\mathcal{C}$ is introduced:

$$y = \mathcal{C}\mathbf{x}, \tag{3.26}$$

where y is the vertical velocity v' of the fluid measured in the body-fixed frame at a fixed

doi:10.6342/NTU202503926

location $x = 1.0D$ downstream of the cylinder. This signal reflects both the flow velocity and the transverse motion of the cylinder. Since the state is represented in vorticity form, the output matrix $\mathcal{C}$ is computed by solving a Poisson equation to recover the velocity at the sensor location.

Transforming the system into the frequency domain yields the input–output relation:

$$\hat{y} = P(s)\hat{u} + \hat{d}, \tag{3.27}$$

where $P(s) = \mathcal{C}(s\mathbf{I} - \mathcal{A})^{-1}\mathcal{B}$ represents the transfer function of the linearized system, and $\hat{d}$ accounts for the spectral effect of nonlinear disturbances on the output.

The resolvent operator $\mathcal{H}(\omega) = (-i\omega\mathbf{I} - \mathcal{A})^{-1}$, introduced in (2.21), characterizes the system's frequency response to harmonic forcing. It directly provides the basis for constructing the reference model $P(s)$ used in the flow control design, as detailed in Section 2.3.

Since the full-order transfer function $P(s)$ is typically ROM is constructed to facilitate practical control implementation. The frequency response of the original system is computed using the MATLAB toolbox *fidfrd*, and a reduced-order model of order less than ten is then identified. This ROM serves as the reference model for the flow control setup, enabling efficient computation while preserving the essential dynamic characteristics needed for effective control.

doi:10.6342/NTU202503926

Chapter 4 Results and Discussion

This chapter presents the results of numerical simulations conducted to evaluate the effectiveness of the proposed model reference adaptive control strategy in mitigating the plunging motion of a circular cylinder under FSI. The primary objective of this study is to reduce both the lift fluctuations and the transverse oscillations of the cylinder, which result from VIV in an unsteady laminar flow environment.

Section 4.1 discusses the baseline FSI dynamics of the uncontrolled cylinder, providing detailed insights into the flow behavior, lift forces, and structural response. This section serves as a reference point for evaluating the effects of control. Section 4.2 presents the results of applying MRAC, including a comparative analysis with the uncontrolled case. The impact of the adaptive controller on lift fluctuations and flow structures is systematically examined to demonstrate the performance and robustness of the proposed method.

4.1 Circular Cylinder under Flow-Structure Interaction

In this section, the dynamics of a circular cylinder undergoing flow–structure interaction are investigated through numerical simulations. Initially, the cylinder is placed in a uniform free-stream flow. After a brief transient period, it begins to oscillate in the

doi:10.6342/NTU202503926

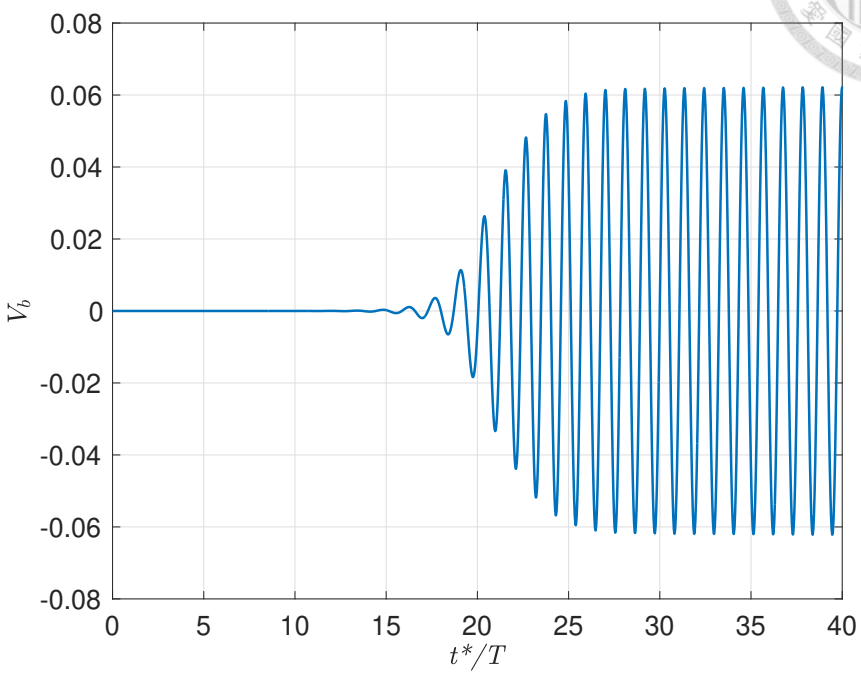

(a)

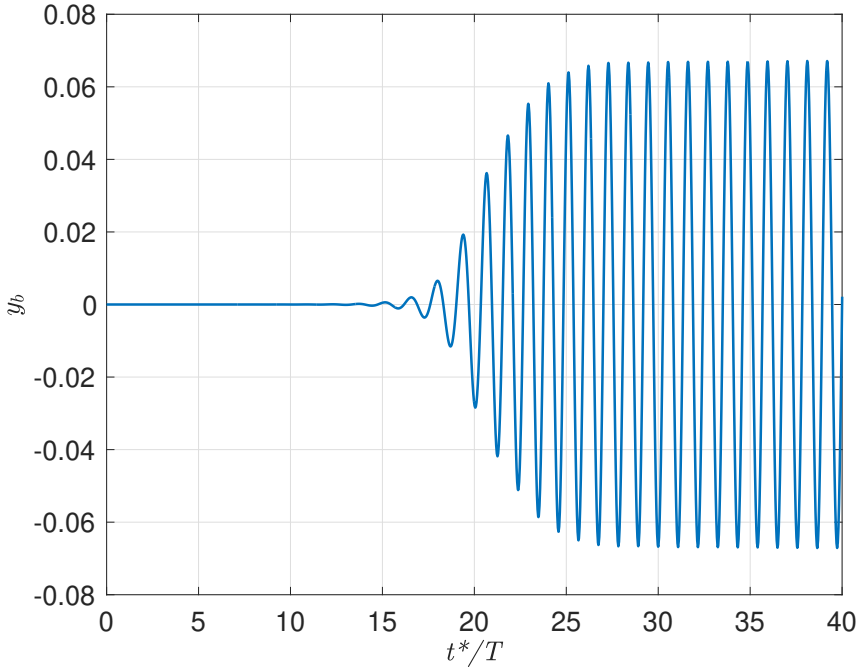

(b)

Figure 4.1: Time histories of (a) the transverse velocity V_b and (b) the position y_b of the cylinder for $\rho_e = 0.2$.

doi:10.6342/NTU202503926

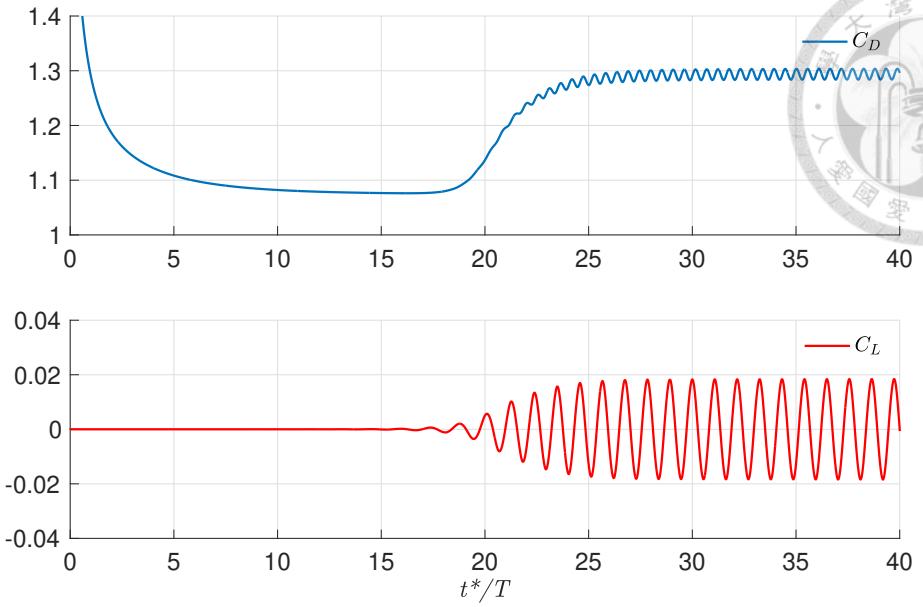

Figure 4.2: Lift coefficient C_L and drag coefficient C_D for $\rho_e = 0.2$.

transverse direction and eventually settles into a periodic plunging motion.

Figure 4.1 shows the evolution of the cylinder's transverse velocity, V_b, and displacement, y_b. Starting from rest, the cylinder gradually develops oscillations in the crossflow direction and soon settles into a stable periodic state. This steady plunging motion persists for more than 10 oscillations. The Strouhal number is defined as $St_p = f_p D/U_\infty$, where f_p denotes the plunging frequency of the cylinder under FSI. The oscillation period, T, is given by $T = 1/St_p$. Time t^* is nondimensionalized by D/U_∞. The corresponding lift coefficient, C_L, and drag coefficient, C_D, are shown in Figure 4.2. The drag coefficient C_D initially decreases and tends to converge near 1.08, but then quickly increases and begins to oscillate with a mean value close to 1.3. The onset of the increase in C_D coincides with the start of oscillations in C_L, and both eventually reach a stable oscillatory state.

Since the motion of the cylinder is strongly coupled with the flow, the effective density ρ_e significantly influences the dynamic response of the system. Figure 4.3 illustrates how the plunging amplitude and frequency vary with ρ_e. As ρ_e increases, the frequency St_p rises slightly from 0.15 to 0.16. For reference, $St_{vs} = 0.16$ denotes the natural vortex-

doi:10.6342/NTU202503926

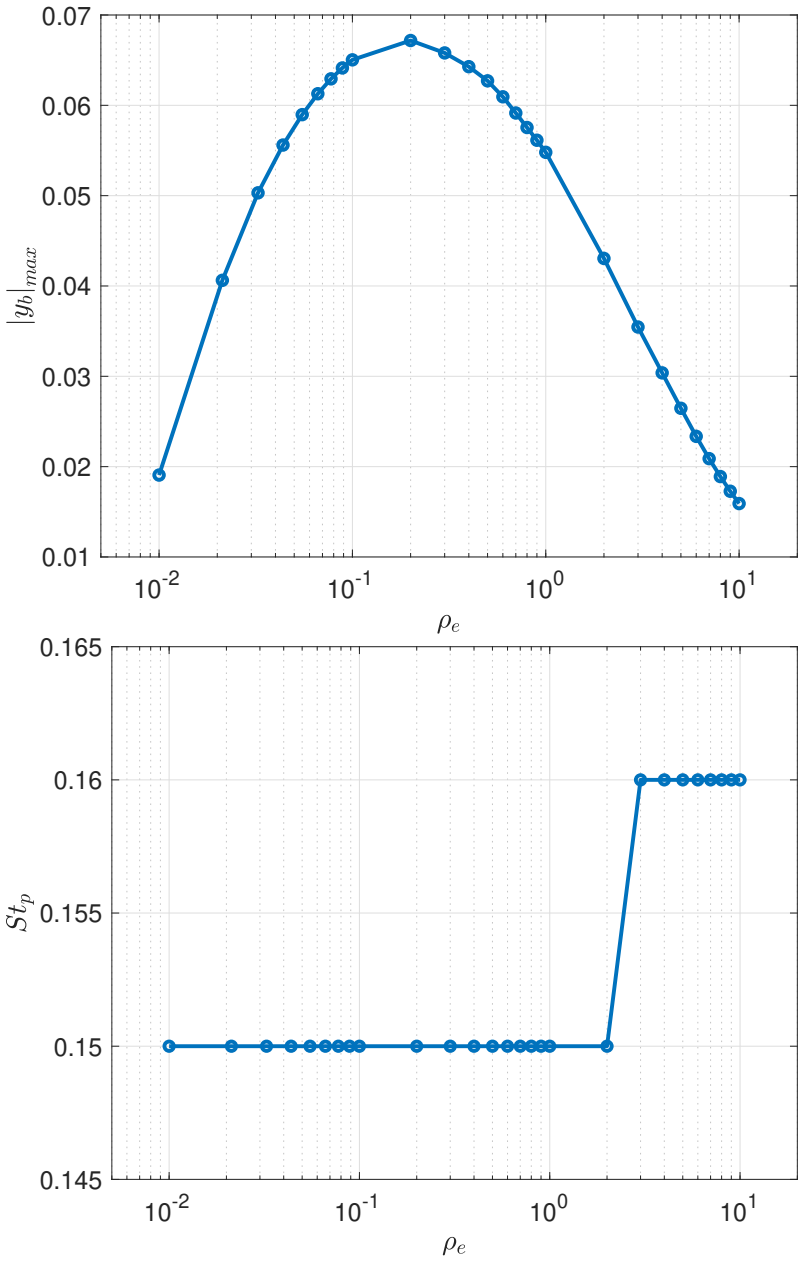

Figure 4.3: Variation of plunging amplitude $|y_b|$ and frequency St_p with effective density ρ_e. The FFT analysis uses a time step of $\Delta t = 0.001$ and 10^5 sample points for spectral resolution.

doi:10.6342/NTU202503926

shedding frequency of a stationary cylinder. The largest plunging amplitude, approximately $|y_b| = 0.65D$, is observed at $\rho_e = 0.2$. Based on this observation, the effective density is set to $\rho_e = 0.2$ for the following analysis, as this condition yields the largest oscillation amplitude and serves as the basis for the controlled flow case.

4.2 Controlled Flow

Since the primary objective of flow control is to reduce the lift fluctuation of the plunging cylinder, which is closely associated with vortex shedding intensity, a new variable is introduced to quantify the control performance. The reduction rate $\mathcal{R}_x$ is defined as

$$\mathcal{R}_x = \frac{\mathcal{S}_x^b - \mathcal{S}_x^c}{\mathcal{S}_x^b}, \tag{4.1}$$

where $\mathcal{S}_x^b$ and $\mathcal{S}_x^c$ are the standard deviations of the time-series data for the baseline (uncontrolled) and controlled cases, respectively. The standard deviation $\mathcal{S}_x$ is computed as

$$\mathcal{S}_x = \sqrt{\frac{1}{N-1}\sum_{i=1}^{N}(x_i - \bar{x})^2}. \tag{4.2}$$

Here, $\bar{x}$ denotes the mean value of the time-series data, and N is the total number of samples. To eliminate the effects of transient response, the time-series data are collected over the final 10 oscillations of the control period, when the system has reached steady behavior. The optimal control setting is determined by the case that provides the largest

doi:10.6342/NTU202503926

reduction rate in fluctuation.

The two parameters, Γ and γ, are hyperparameters that need to be specified before applying control. These learning rates determine the adaptation speed of the adaptive gain vector $\boldsymbol{\theta}_c$ and the parameter ρ, respectively. Since Γ governs the adaptation of $\boldsymbol{\theta}_c$, it has a direct impact on the convergence speed of the controller. While a larger value of Γ can accelerate adaptation, it also increases the risk of instability. Therefore, selecting an appropriate range for (Γ, γ) is essential to ensure both stability and robustness of the control system.

4.2.1 Normal Actuation

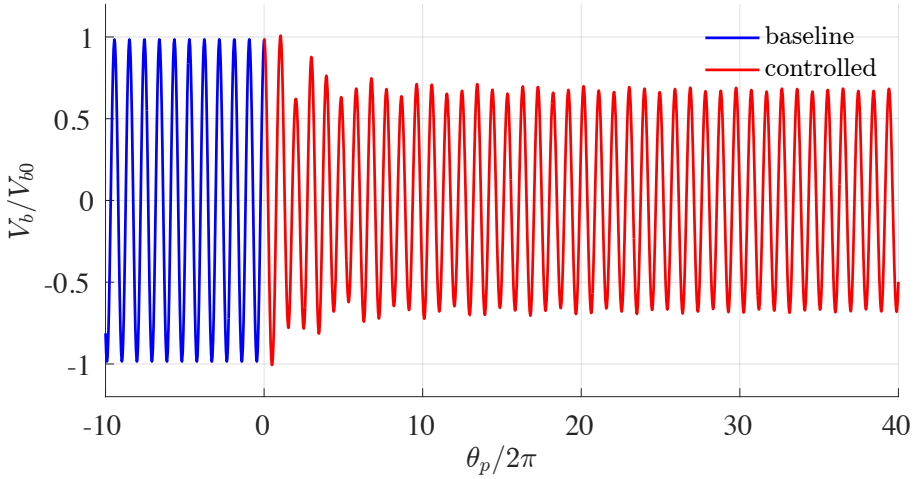

Figure 4.4: Time history of V_b with $(\Gamma, \gamma) = (4, 0.1)$.

For normal actuation, various hyperparameter pairs (Γ, γ) were tested, with $(4, 0.1)$ chosen for demonstration. The oscillation phase θ_p is defined as $\theta_p/2\pi = St_c U_\infty/D$, where St_c denotes the Strouhal number of the cylinder under controlled flow. Figure 4.4 shows the time history of the transverse velocity V_b, with V_{b0} representing the amplitude of the uncontrolled cylinder. The controlled cylinder's transverse velocity gradually decreases and settles into a steady oscillation with diminished amplitude after approximately

doi:10.6342/NTU202503926

$\theta_p/2\pi = 10$. This reduced oscillation amplitude is maintained up to $\theta_p/2\pi = 40$, indicating sustained suppression of transverse velocity fluctuations over more than 30 oscillation cycles. The reduction rate, $R_{V_b} = 32.37\%$, reflects a noticeable decrease in cylinder motion fluctuations, effectively stabilizing the system.

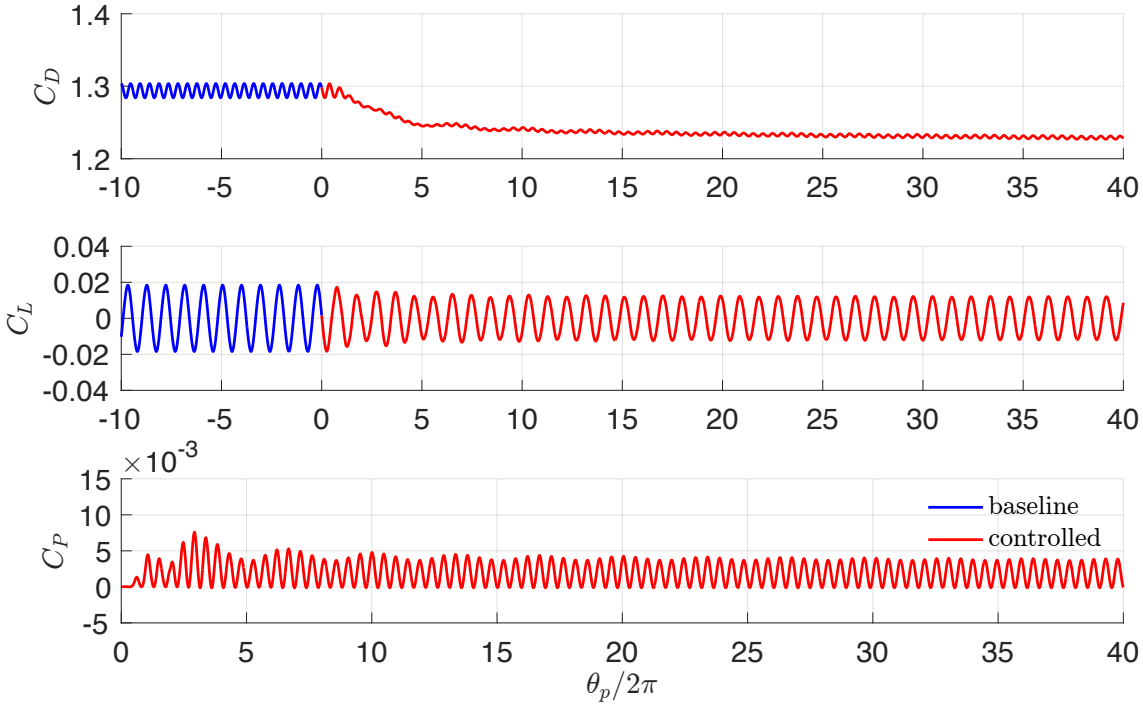

Figure 4.5: Time history of C_D, C_L and C_P with $(\Gamma, \gamma) = (4, 0.1)$.

Figure 4.5 displays trends consistent with those observed in V_b. The lift coefficient C_L follows a similar pattern to V_b, showing decreased oscillations with small amplitude. The drag coefficient C_D decreases smoothly and converges to approximately 1.23 with minor oscillations after $\theta_p/2\pi = 10$. The power coefficient C_p, representing control efficiency, remains consistently below 10^{-2} throughout the control period, indicating minimal energy consumption. Overall, the reductions achieved in lift and drag fluctuations ($R_L = 34.22\%$, $R_D = 74.22\%$) highlight the effectiveness of normal actuation combined with the proposed control strategy in attenuating force oscillations.

Figure 4.6 illustrates the evolution of the adaptive gains $\boldsymbol{\theta}_c$ and the cost function J during the control period. The adaptive gains change rapidly within the interval $\theta_p/2\pi \in$

doi:10.6342/NTU202503926

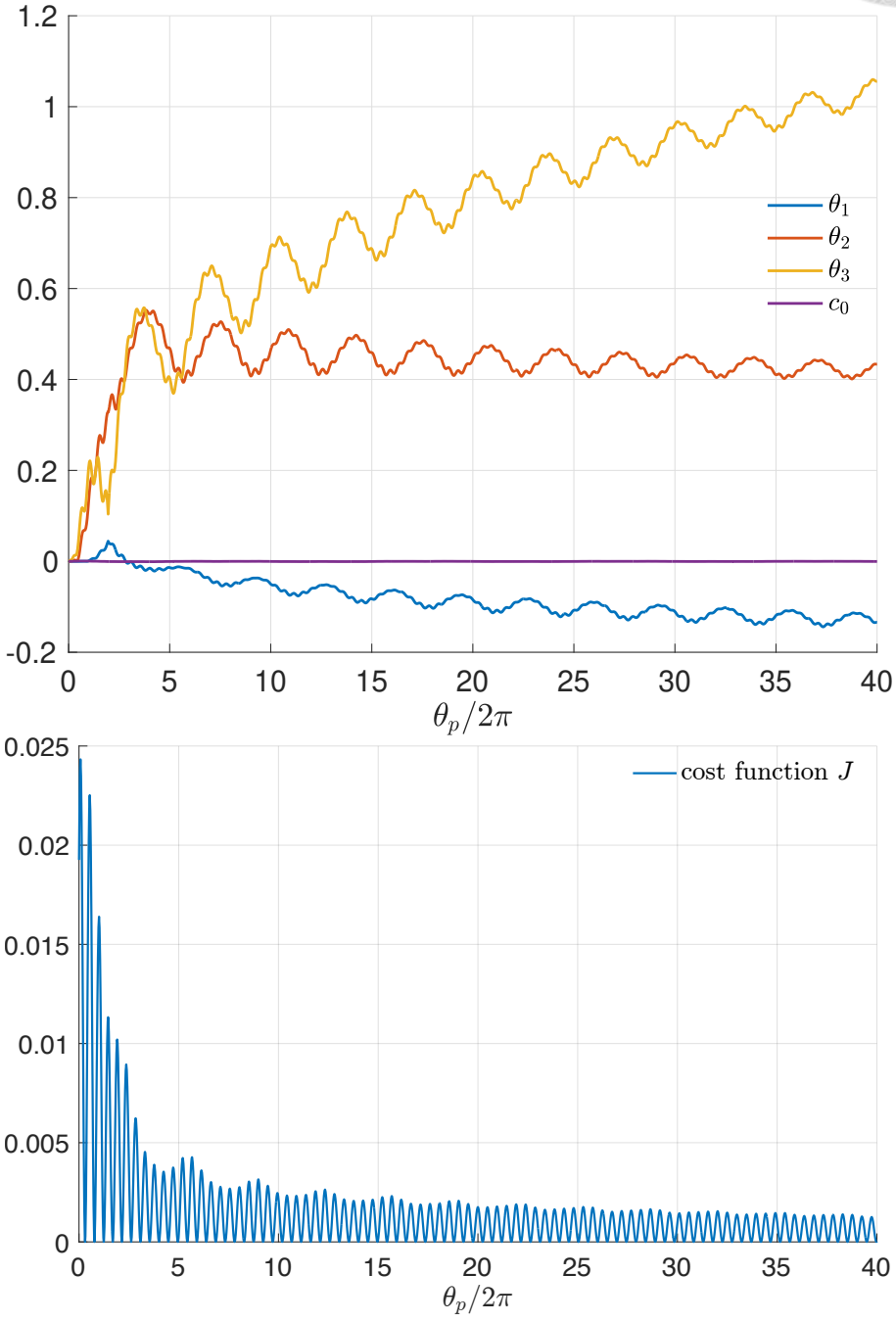

Figure 4.6: Time history of adaptive gain $\boldsymbol{\theta}_c$ and cost function J with $(\Gamma, \gamma) = (4, 0.1)$.

doi:10.6342/NTU202503926

$[0, 5]$, then oscillate with small amplitude around a near-constant value. The cost function decreases rapidly as the control activates, exhibiting small residual oscillations. This behavior corresponds closely with the trends observed in V_b and C_L, indicating stable actuation accompanied by minor fluctuations in the adaptive gains. According to adaptive control theory, the gains should converge to constant values in a linear system. However, the FSI system during stable plunging retains nonlinear effects, resulting in slight residual oscillations even after the system appears to have reached steady state.

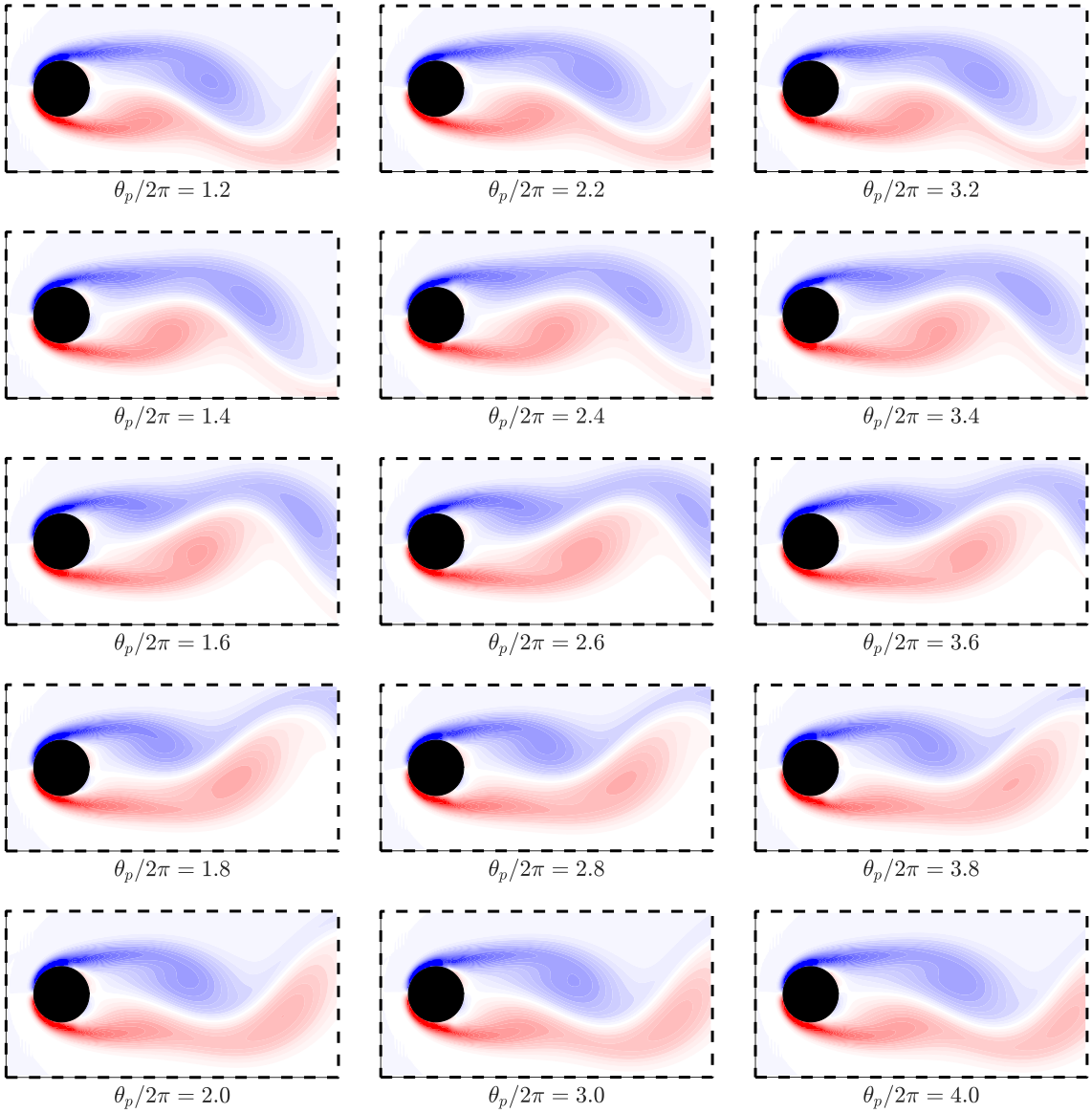

Figure 4.7: Vorticity snapshots over three oscillation cycles for $\theta_p/2\pi \in [1, 4]$. From top to bottom, snapshots are taken at intervals of $\Delta(\theta_p/2\pi) = 0.2$, illustrating the evolution of the wake vorticity. The vorticity remains nearly consistent with that of the baseline case under FSI.

doi:10.6342/NTU202503926

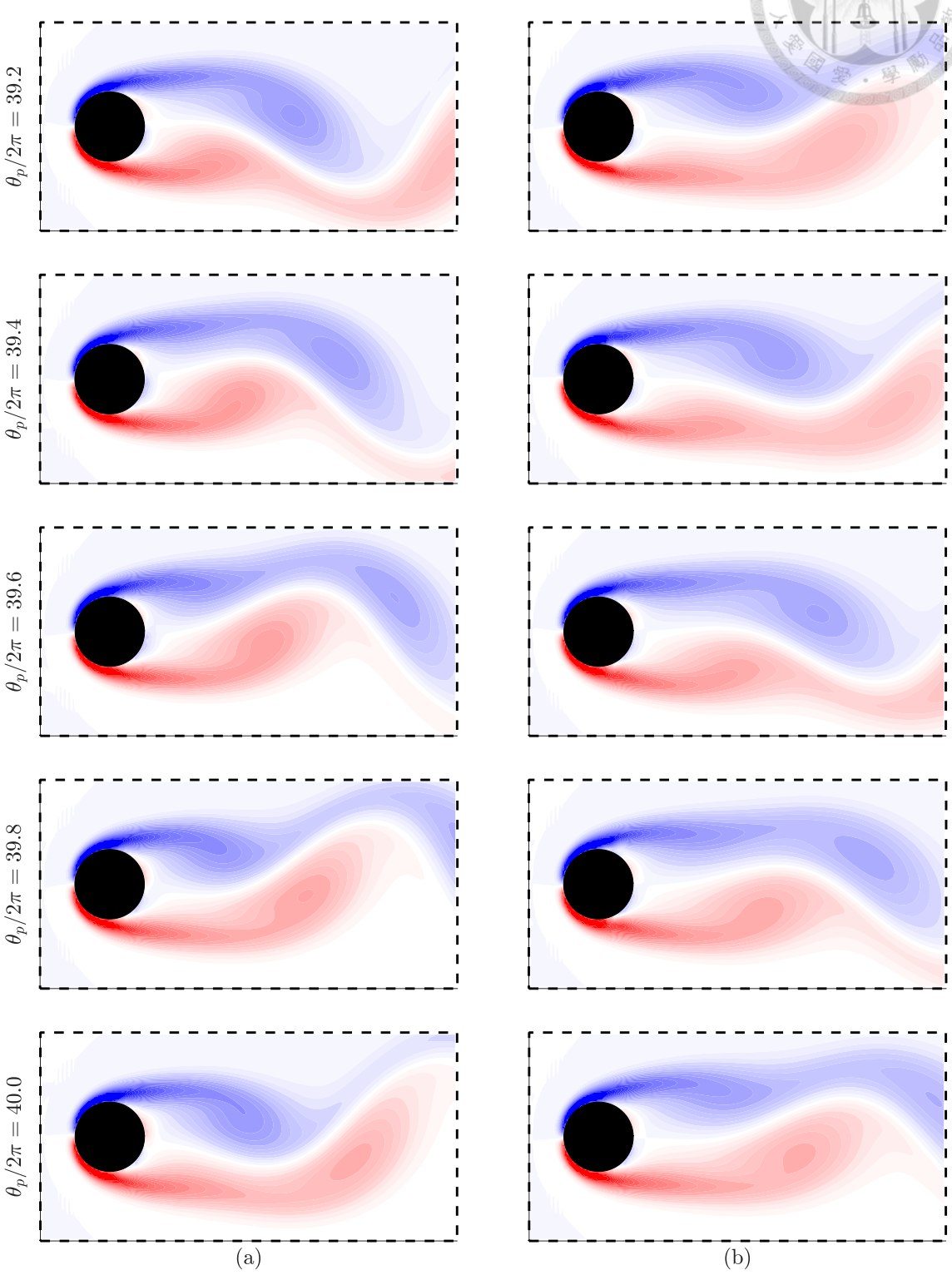

Figure 4.8: Vorticity snapshots over the final oscillation, $\theta_p/2\pi \in [39, 40]$, comparing (a) the baseline and (b) the controlled flow.

doi:10.6342/NTU202503926

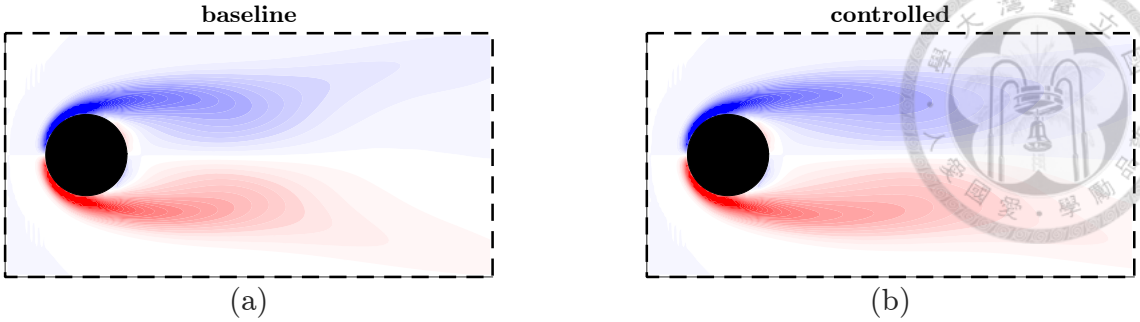

(a) (b)

Figure 4.9: Comparison of the time-averaged vorticity fields for the baseline (a) and controlled (b) cases, computed over the interval $\theta_p/2\pi \in [30, 40]$.

Figure 4.7 shows vorticity snapshots at $\theta_p/2\pi \in [1, 4]$. The wake structure behind the cylinder remains consistent with that of the baseline case under flow–structure interaction (FSI). The actuation primarily influences the cylinder dynamics, while the intensity of vortex shedding remains nearly unchanged. This observation is supported by the vorticity over the final 10 oscillations, as shown in Figure 4.8. Figure 4.9 displays the time-averaged vorticity over $\theta_p/2\pi \in [30, 40]$, revealing a slight downstream elongation of the wake. This elongation is attributed to a modest shift in the plunging frequency of the cylinder under controlled flow compared to the baseline case.

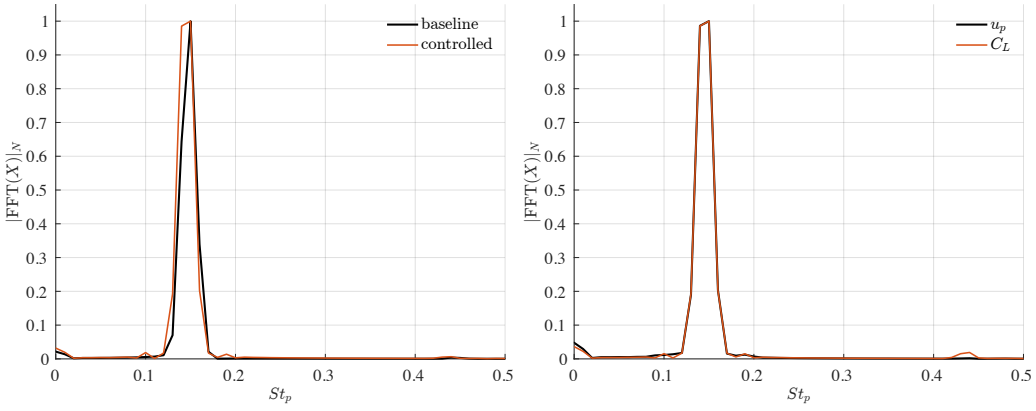

(a) (b)

Figure 4.10: FFT spectra of (a) the transverse velocity V_b for the baseline and controlled flow cases, and (b) the control input u_p alongside the lift coefficient C_L. The amplitude of the FFT spectra is normalized by the maximum amplitude. The spectra of u_p and C_L exhibit strong lock-in. The lift coefficient C_L shows the same dominant frequency as V_b. The FFT analysis uses a time step of $\Delta t = 0.001$ and 10^5 sample points for spectral resolution.

Figure 4.10 presents the FFT analysis of the plunging motion and the control input.

doi:10.6342/NTU202503926

The spectra of the control input u_p and the plunging motion exhibit strong lock-in, indicating synchronization between the actuation and the fluid response. The two dominant peaks in the spectrum occur at frequencies close to 0.15, reflecting consistent oscillatory behavior. This corresponds to a reduction in oscillation amplitude under control.

The control is activated at different phases of the plunging motion to verify that effective performance is achieved regardless of the timing of engagement. Additionally, the control is switched on and off multiple times to demonstrate its long-term consistency. In these simulations, the controller operates with the same parameter pair $(\Gamma, \gamma) = (4, 0.1)$.

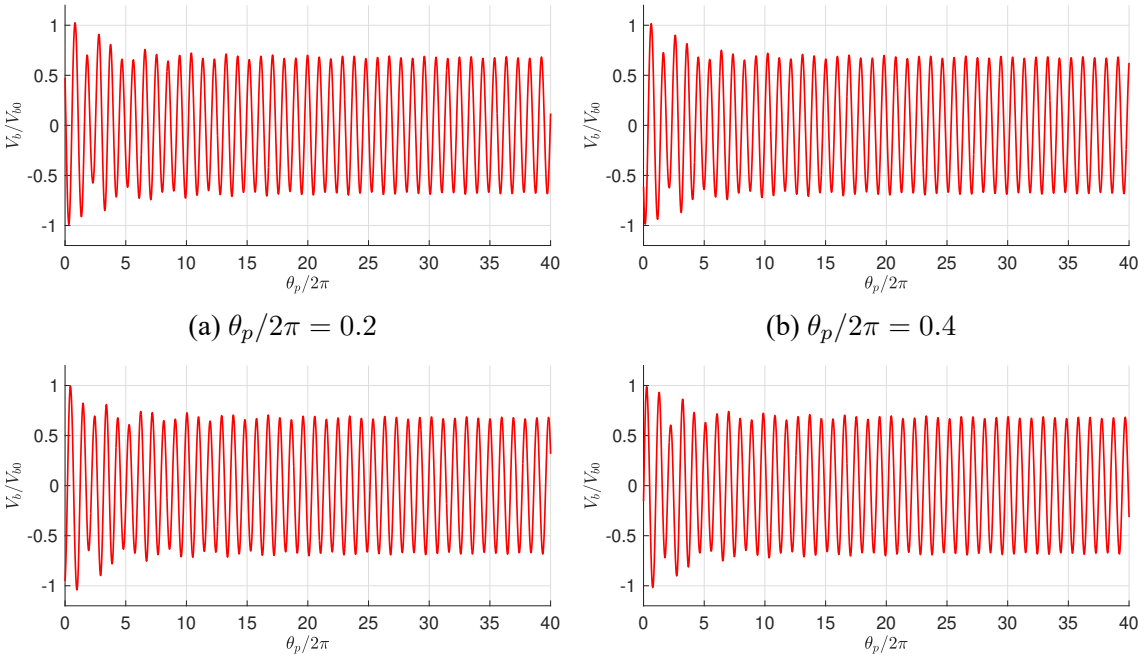

(a) $\theta_p/2\pi = 0.2$ (b) $\theta_p/2\pi = 0.4$

(c) $\theta_p/2\pi = 0.6$ (d) $\theta_p/2\pi = 0.8$

Figure 4.11: Time histories of V_b under optimal learning rates $(\Gamma, \gamma) = (4, 0.1)$ for control activated at different phases $\theta_p/2\pi$: (a) 0.2, (b) 0.4, (c) 0.6, and (d) 0.8. Each case demonstrates consistent fluctuation reduction regardless of activation phase.

Figure 4.11 compares V_b responses when control is activated at different phases $\theta_p/2\pi$.The long-term reduction in fluctuation remains the same. After 10 oscillations, the flow fluctuations converge to a consistent, stable level regardless of the phase at which control was applied.

doi:10.6342/NTU202503926

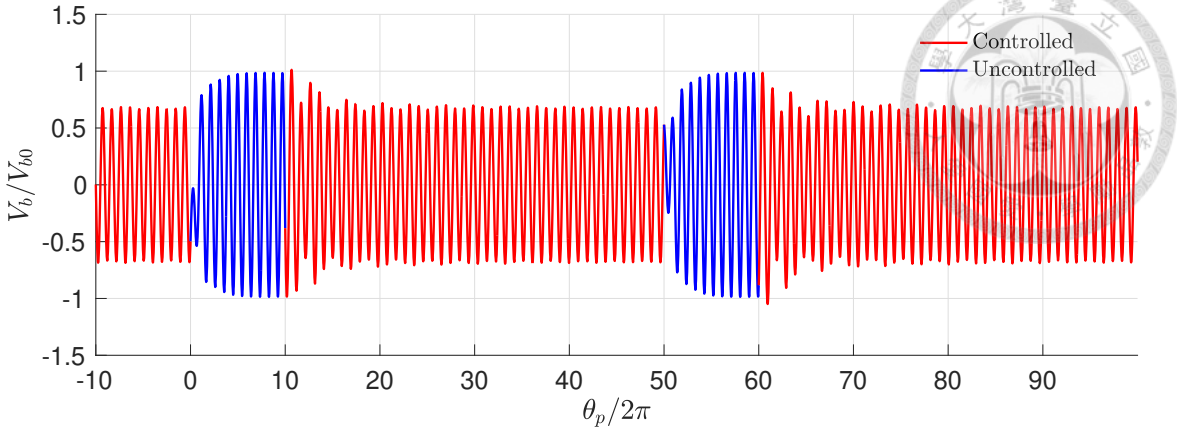

Figure 4.12: Time histories of the cylinder's transverse velocity V_b over three cycles of control activation and deactivation. Time is referenced from the start of the second control period. Each control phase is followed by a 10-oscillation interval with the control off, during which V_b returns to the baseline behavior under FSI. Upon reactivation, the control consistently achieves effective suppression of V_b fluctuations, with similar transient responses observed across all cycles.

Figure 4.12 presents the results of three cycles of control turn on and off. Between each controlled period, the control is switched off, allowing the system to evolve freely for at least 5 oscillations. During these off intervals, the amplitude of the cylinder's transverse velocity V_b increases and returns to levels observed in the baseline case. When the control is reactivated, the reduction in V_b during each control period remains nearly consistent. The first period corresponds to the previously reported results, shown as the plot of the final 10 oscillations, while the second and third periods achieve almost identical reduction rates. The repeated control intervals with the same settings exhibit consistent effectiveness in suppressing fluctuations, demonstrating the robustness of the adaptive control strategy.

Figure 4.13 illustrates the moderate ranges for the adaptive parameters (Γ, γ). Within the tested domain $(\Gamma, \gamma) \in [0.01, 8] \times [0.0001, 0.1]$, the model reference adaptive control achieves notable reductions in both the lift coefficient C_L and the transverse velocity V_b. The optimal parameter pair $(\Gamma, \gamma) = (4, 0.1)$ provides the greatest suppression of fluctuations, with maximum reductions of $\mathcal{R}_L = 34.22\%$ in lift coefficient fluctuation and $\mathcal{R}_{V_b} = 32.37\%$ in transverse velocity fluctuation. The reduction in drag coefficient is

doi:10.6342/NTU202503926

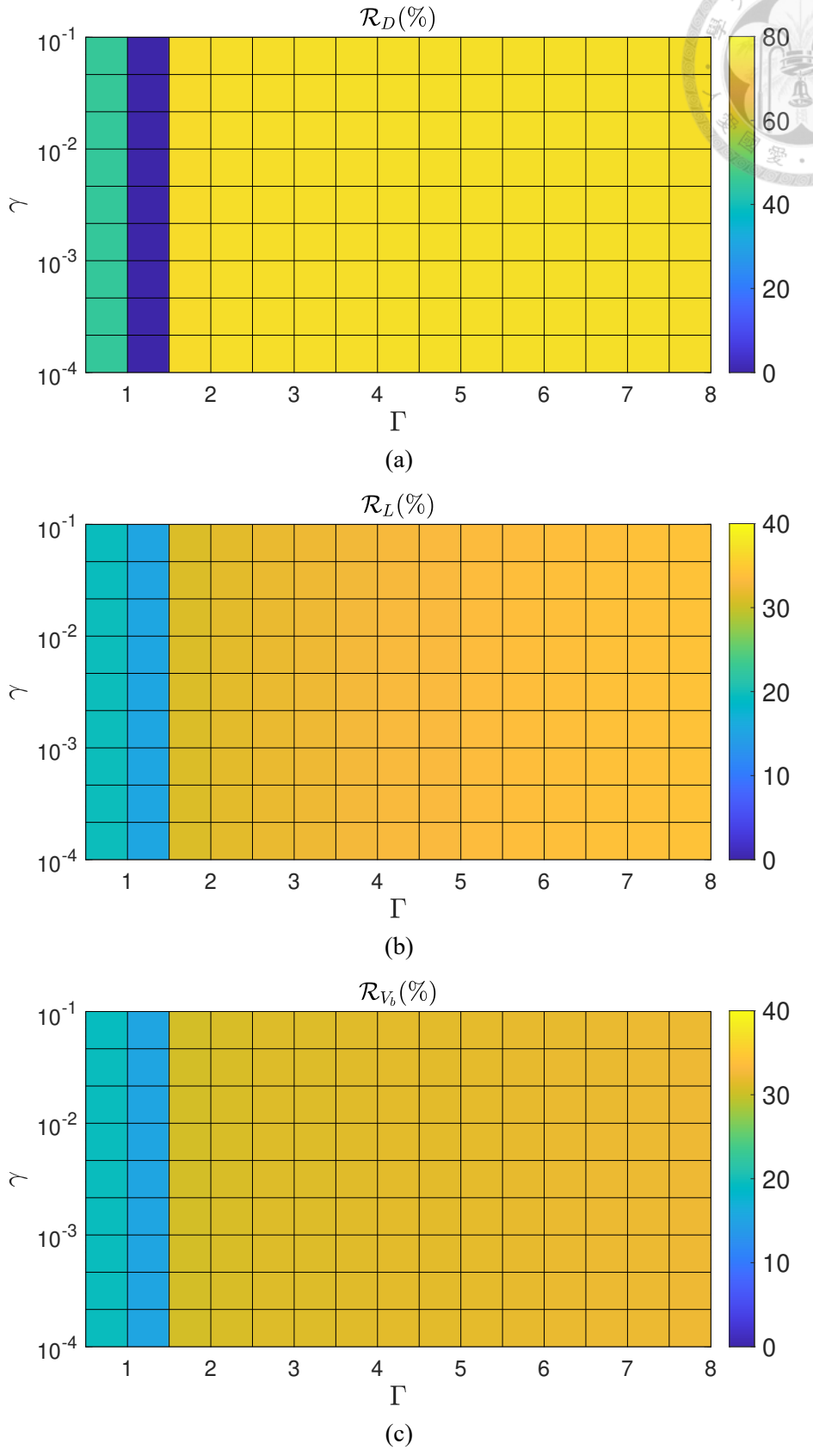

Figure 4.13: Reduction rates of (a) drag fluctuation $\mathcal{R}_D$, (b) lift fluctuation $\mathcal{R}_L$, and (c) transverse velocity fluctuation $\mathcal{R}_{V_b}$ across the (Γ, γ) parameter space $\Gamma \in [0.01, 10], \gamma \in [10^{-2}, 10^{2}]$.

doi:10.6342/NTU202503926

$R_D = 74.22\%$. Control performance is primarily influenced by Γ, which governs the adaptation rate of the adaptive gains $\boldsymbol{\theta}_c$, while γ mainly affects the transient response, with smaller values potentially causing instability. Overall, the adaptive control demonstrates robust and effective performance across a broad range of these parameters.

4.2.2 Tangential Actuation

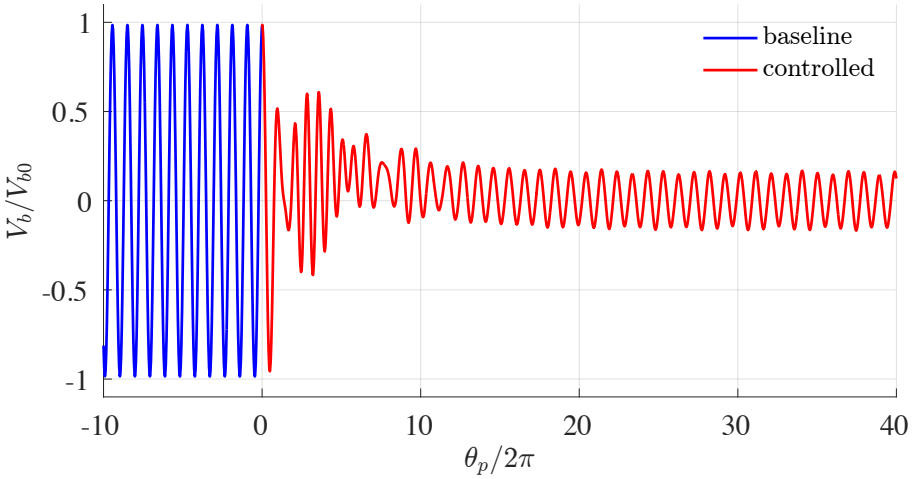

Figure 4.14: Time history of V_b with $(\Gamma, \gamma) = (0.76, 100)$.

A range of hyperparameter pairs (Γ, γ) was tested, and the pair $(\Gamma, \gamma) = (0.76, 100)$ was chosen for demonstration. Figure 4.14 shows the time history of V_b, where V_{b0} denotes the amplitude of the transverse velocity of the uncontrolled cylinder. During the initial 10 oscillations, ($\theta_p/2\pi \in [0, 10]$), the amplitude of V_b decreases rapidly with unstable fluctuations, although these remain smaller than the baseline. After $\theta_p/2\pi = 10$, the amplitude stabilizes and remains steady up to $\theta_p/2\pi = 40$, indicating that the reduction in V_b is sustained for more than 30 oscillations. The reduction rate $R_{V_b} = 84.36\%$ represents a significant decrease in fluctuations of the cylinder motion, effectively stabilizing the cylinder.

Figure 4.15 presents the time histories of force and power coefficients during control.

doi:10.6342/NTU202503926

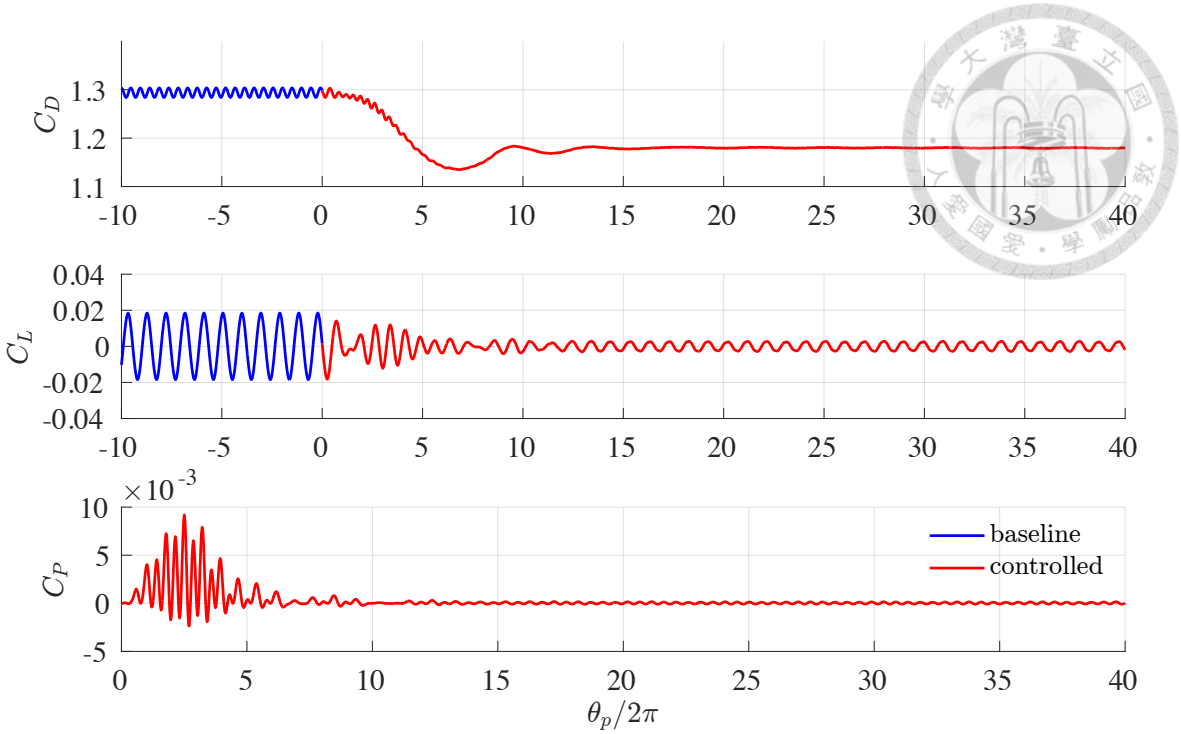

Figure 4.15: Time history of C_D, C_L and C_P with $(\Gamma, \gamma) = (0.76, 100)$.

The lift coefficient C_L stabilizes rapidly after $\theta_p/2\pi = 10$, exhibiting a substantial reduction in fluctuations. Concurrently, the drag coefficient C_D initially decreases smoothly, experiences a minor rebound to approximately 1.2 at $\theta_p/2\pi = 10$, and subsequently converges steadily to around 1.18—representing a significant 10% decrease in its average magnitude. Both the mean value and fluctuation amplitude of C_D are markedly diminished. The total power coefficient C_p of the two actuators remains consistently below 10^{-3} throughout the control interval and decreases further after $\theta_p/2\pi = 10$. The reductions in lift and drag fluctuations ($R_L = 84.96\%$, $R_D = 92.67\%$) demonstrate the effectiveness of the proposed control strategy in diminishing force oscillations.

Figure 4.16 illustrates the evolution of the adaptive gains $\boldsymbol{\theta}_c$ during the control period. The gains adjust rapidly at the onset of control and subsequently oscillate around nearly constant values. The cost function decreases rapidly upon activation of the control, eventually approaching zero, indicating that the fluid system closely tracks the reference model and effectively reduces fluctuations. This trend aligns closely with the behaviors

doi:10.6342/NTU202503926

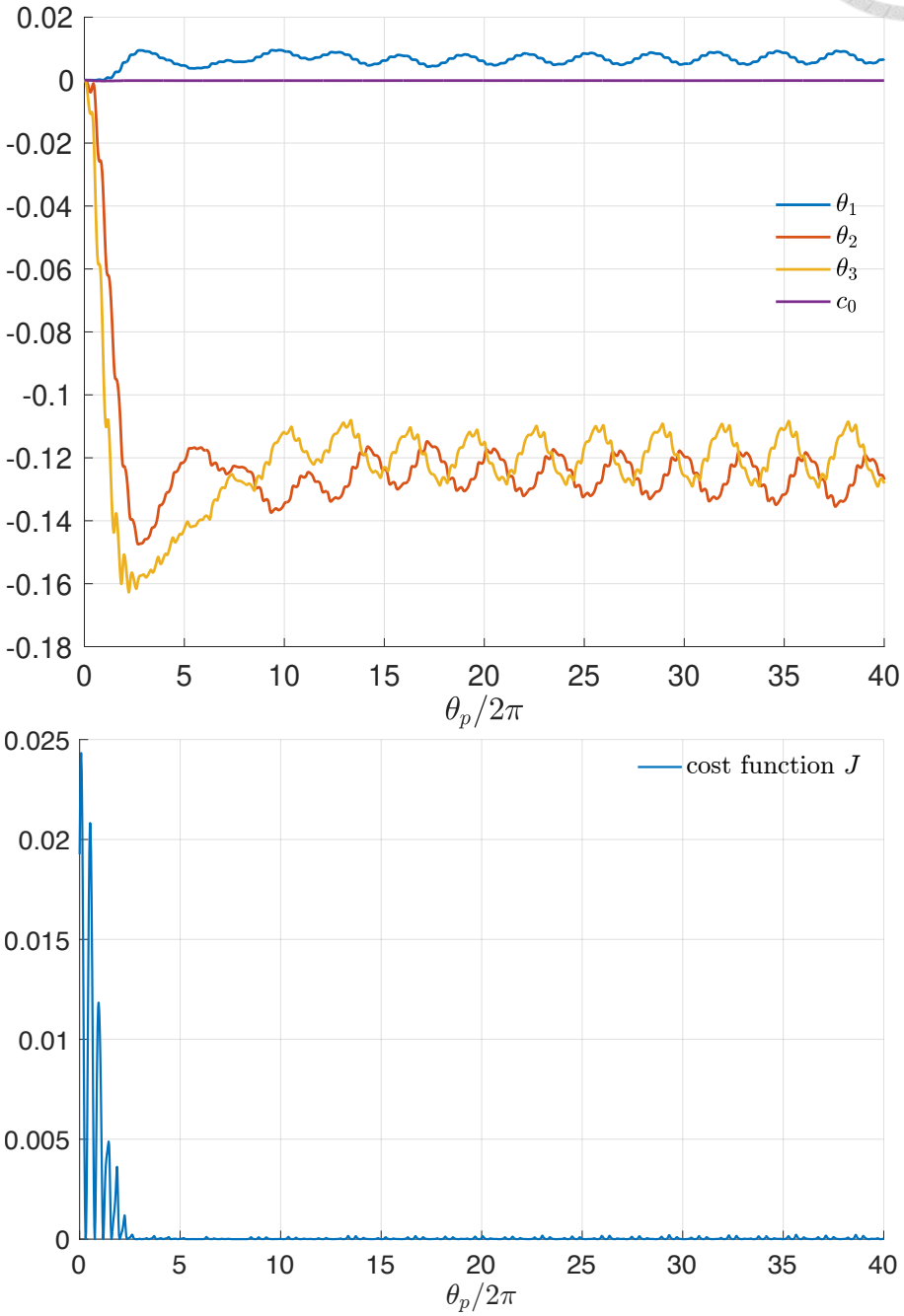

Figure 4.16: Time history of adaptive gain $\boldsymbol{\theta}_c$ and cost function J with $(\Gamma, \gamma) = (0.76, 100)$.

doi:10.6342/NTU202503926

observed in V_b and C_L, demonstrating stable actuation accompanied by minor fluctuations in the adaptive gains. According to adaptive control theory, the gains should converge to constant values in a linear system. However, the FSI system under stable plunging retains nonlinear interactions, resulting in small residual oscillations even after the system appears to reach steady state.

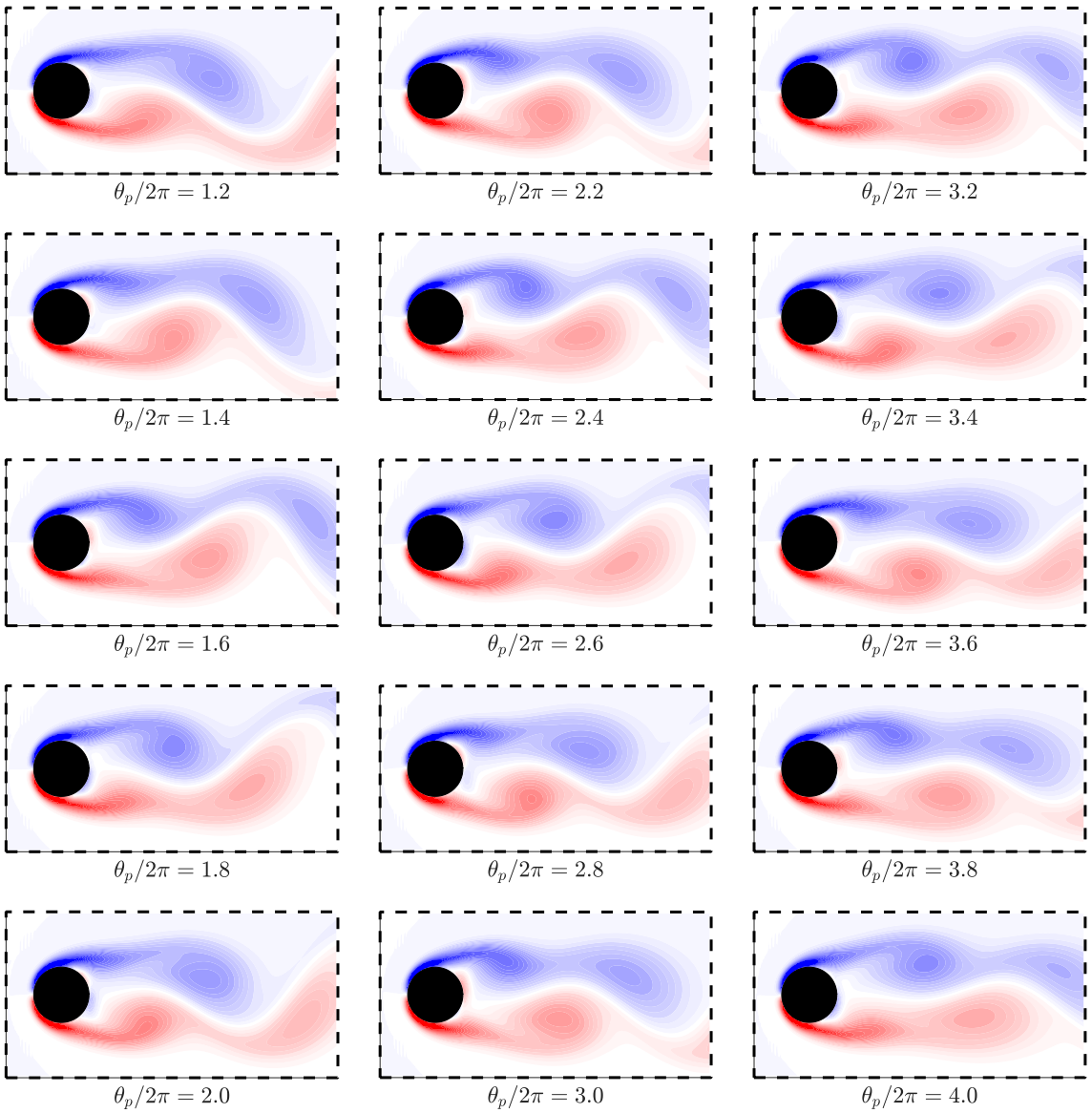

Figure 4.17: Vorticity snapshots over three oscillation cycles for $\theta_p/2\pi \in [1, 4]$. From top to bottom, snapshots are taken at intervals of $\Delta(\theta_p/2\pi) = 0.2$, illustrating the evolution of the wake vorticity. The activation of control alters vortex shedding behind the cylinder.

Figure 4.17 presents vorticity snapshots at the start of the control period. Under actuation, the wake vortices behind the cylinder break down into smaller-scale structures,

doi:10.6342/NTU202503926

reducing vorticity intensity in the near wake. This transition coincides with the interval of peak actuation observed in the plot of C_P in Figure 4.15. The control input thus alters the vortex pattern in the wake, attenuating flow-induced fluctuations on the cylinder and quickly stabilizing the flow.

Figure 4.18 shows vorticity snapshots for the base plunging and controlled cases during the final oscillation ($\theta_p/2\pi \in [39, 40]$). With actuation, the wake exhibits reduced vorticity intensity and extends farther downstream compared to the baseline case. This elongation reduces the wake's direct influence on the cylinder, leading to smaller amplitude fluctuations. The more diffuse wake indicates a broader vorticity distribution, reducing the intensity of individual vortices. Figure 4.19 presents the time-averaged vorticity over the final 10 oscillations, further highlighting the stretched wake structure.

Figure 4.20 presents the FFT analysis of both the baseline case and the controlled flow. The spectra of the control input u_p and the lift coefficient C_L exhibit strong lock-in, indicating synchronization between the actuation and the response of the fluid system. The lift coefficient C_L oscillates at the same dominant frequency as the transverse velocity V_b. This behavior corresponds to a reduction in oscillation amplitude, demonstrating that the fluid system transitions to a state with diminished fluctuations under control.

The control is switched on and off multiple times to demonstrate long-term consistency. Additionally, it is activated at different phases of the plunging motion to verify that effective performance is achieved regardless of the timing of engagement.

Figure 4.21 compares V_b responses when control is activated at different phases $\theta_p/2\pi$. Although the activation phase alters the transient response during the first ten oscillations ($\theta_p/2\pi \in [0, 10]$), the long-term reduction in fluctuation remains the same. After

doi:10.6342/NTU202503926

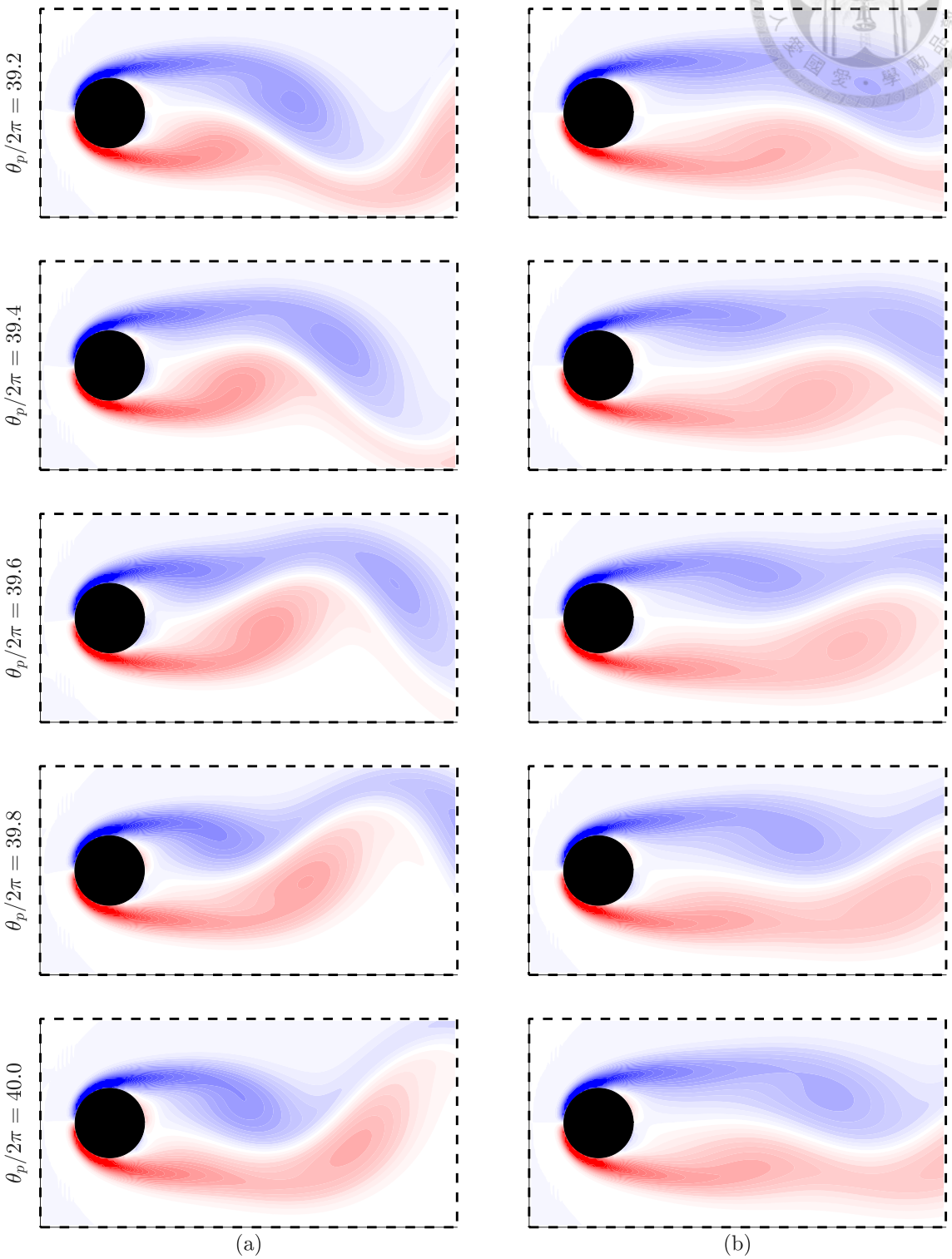

Figure 4.18: Vorticity snapshots over the final oscillation, $\theta_p/2\pi \in [39, 40]$, comparing (a) the baseline and (b) the controlled case. The controlled wake shows reduced vorticity intensity and elongated structures downstream, indicating suppression of vortex shedding.

doi:10.6342/NTU202503926

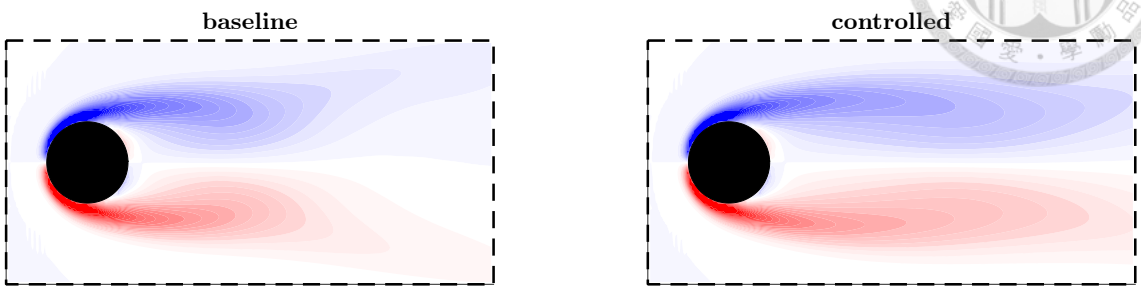

(a) (b)

Figure 4.19: Comparison of the time-averaged vorticity fields for the baseline (a) and controlled (b) cases, computed over the interval $\theta_p/2\pi \in [30, 40]$. The controlled case exhibits reduced vorticity intensity and a more elongated wake structure downstream, indicating effective suppression of vortex shedding.

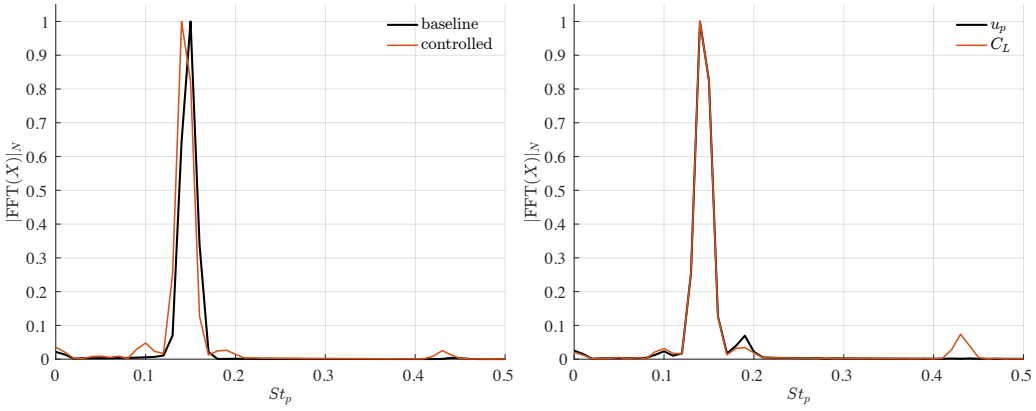

(a) (b)

Figure 4.20: FFT spectra of (a) the transverse velocity V_b for the baseline and controlled flow cases, and (b) the control input u_p alongside the lift coefficient C_L. The amplitude of the FFT spectra is normalized by the maximum amplitude. The spectra of u_p and C_L exhibit strong lock-in. The lift coefficient C_L shows the same dominant frequency as V_b. The FFT analysis uses a time step of $\Delta t = 0.001$ and 10^5 sample points for spectral resolution.

doi:10.6342/NTU202503926

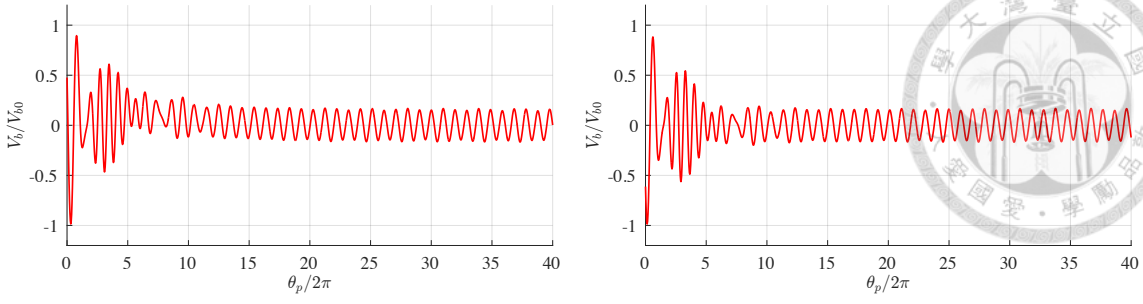

(a) $\theta_p/2\pi = 0.2$ (b) $\theta_p/2\pi = 0.4$

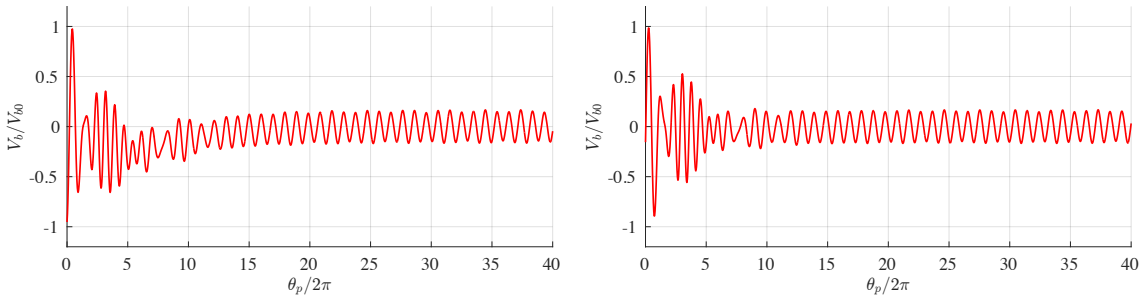

(c) $\theta_p/2\pi = 0.6$ (d) $\theta_p/2\pi = 0.8$

Figure 4.21: Time histories of V_b for control activated at different phases $\theta_p/2\pi$: (a) 0.2, (b) 0.4, (c) 0.6, and (d) 0.8. Each case demonstrates consistent fluctuation reduction regardless of activation phase.

10 oscillations, the flow fluctuations converge to a consistent, stable level regardless of the phase at which control was applied.

Figure 4.22 shows the results for three cycles of control activation and deactivation. Between each control period, the control is switched off, allowing the system to evolve freely for at least 5 oscillations. During these off intervals, the amplitude of the cylinder's transverse velocity V_b increases and returns to the levels observed in the baseline case. The control is then turned on again at the same phase of the plunging motion as the previous activation. In each control period, the reduction in the cylinder's transverse velocity V_b remains highly consistent. The first period corresponds to the previously reported results, while the second and third periods achieve nearly identical reduction rates. The reduction in lift fluctuations is also nearly identical across all control intervals. Furthermore, the time history of the adaptive gain demonstrates convergence toward the same values during each control period, with only small residual oscillations.

doi:10.6342/NTU202503926

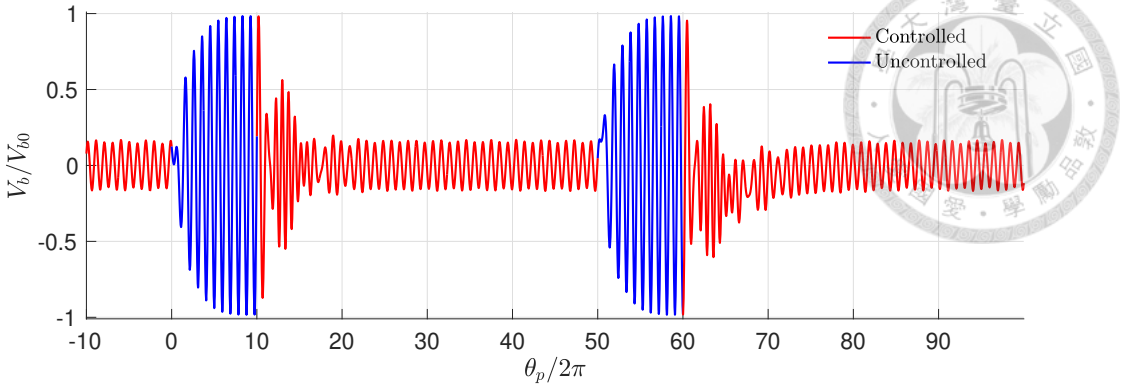

Figure 4.22: Time histories of the cylinder's transverse velocity V_b over three cycles of control activation and deactivation. Time is referenced from the start of the second control period. Each control phase is followed by a 10-oscillation interval with the control off, during which V_b returns to the baseline behavior under FSI. Upon reactivation, the control consistently achieves effective suppression of V_b fluctuations, with similar transient responses observed across all cycles.

Figure 4.23 illustrates the moderate ranges for the adaptive parameters (Γ, γ). Within the tested domain $(\Gamma, \gamma) \in [0.01, 10] \times [0.01, 100]$, the adaptive control with tangential actuation achieves substantial reductions in both the lift coefficient C_L and the transverse velocity V_b. The optimal parameter pair $(\Gamma, \gamma) = (0.76, 100)$ yields the greatest suppression of fluctuations, with maximum reductions of 84.96% in lift coefficient fluctuation $\mathcal{R}_L$ and 84.36% in transverse velocity fluctuation $\mathcal{R}_{V_b}$. The drag coefficient fluctuation is also significantly reduced by $\mathcal{R}_D = 92.67\%$ at this optimal setting. Control performance is primarily influenced by Γ, which governs the updating rate of the adaptive gains $\boldsymbol{\theta}_c$, while γ affects the transient response, with smaller values potentially leading to instability. Overall, the adaptive control demonstrates effective and robust performance across a wide range of these parameters.

doi:10.6342/NTU202503926

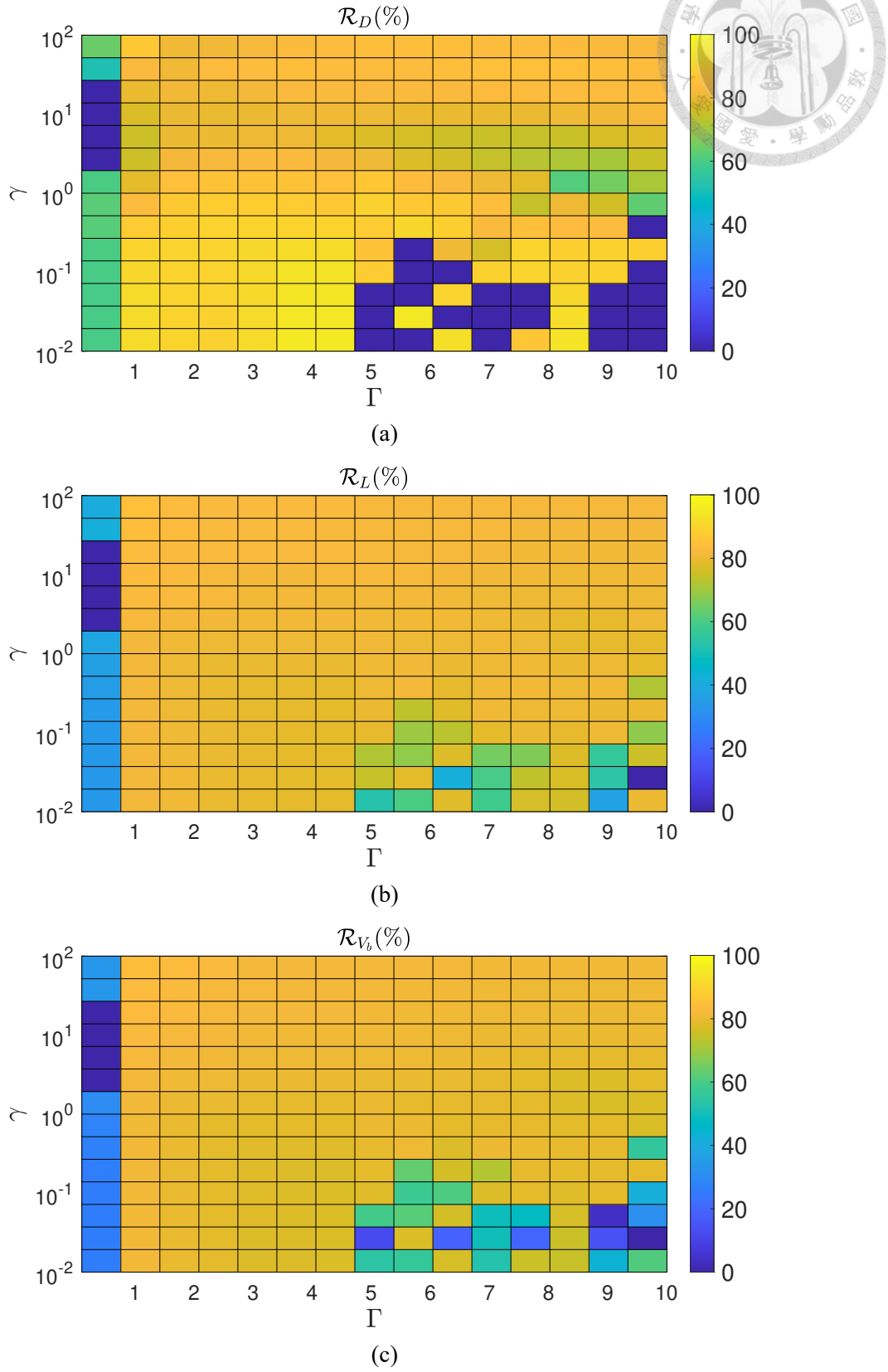

Figure 4.23: Reduction rates of (a) drag fluctuation $\mathcal{R}_D$, (b) lift fluctuation $\mathcal{R}_L$, and (c) transverse velocity fluctuation $\mathcal{R}_{V_b}$ across the (Γ, γ) parameter space $\Gamma \in [0.01, 10], \gamma \in [10^{-2}, 10^2]$.

doi:10.6342/NTU202503926

Chapter 5 Conclusion and Remarks

In this study, we developed a feedback flow control strategy aimed at mitigating vortex-induced fluctuations and stabilizing the plunging dynamics of a circular cylinder undergoing flow–structure interaction. The uncontrolled baseline plunging is characterized by pronounced fluctuations in both the lift force and transverse motion of the cylinder, driven primarily by periodic vortex shedding in the cylinder wake. To suppress these fluctuations, we proposed a model reference adaptive control framework utilizing a linear reference model derived from resolvent analysis of the time-averaged flow around a stationary cylinder—considered a base state with minimal fluctuations. The control law includes two adaptive learning rates as hyperparameters, which govern the transient response and convergence properties of the controller. Normal and tangential actuation schemes were implemented and evaluated to assess their effectiveness in controlling the coupled fluid–structure dynamics.

The adaptive learning rates provided stable and effective control across a suitable range for both actuation schemes. For normal actuation, the adaptive controller achieved maximum reductions of 34.22% in lift coefficient fluctuations, 32.37% in cylinder transverse velocity fluctuations, and 74.22% in drag coefficient fluctuations. Normal actuation directly influenced the cylinder's motion, consequently enhancing nonlinear forcing effects within the coupled system. In contrast, tangential actuation demonstrated substan-

doi:10.6342/NTU202503926

tially superior performance, achieving reductions of 84.96% in lift fluctuations, 84.36% in cylinder transverse velocity fluctuations, and 92.67% in drag coefficient fluctuations.

During the transient period of control implementation, the system initially exhibited notable fluctuations but rapidly stabilized, achieving substantially reduced oscillations for both actuation schemes. Under normal actuation, the vortex structure behind the cylinder exhibited only minor modifications, indicating that control primarily influenced the cylinder motion rather than directly altering wake structures. Conversely, tangential actuation caused the rapid breakdown of near-wake vortex structures into smaller-scale patterns during the early transient stage, a phenomenon not prominently observed under normal actuation. After approximately ten oscillations, both actuation schemes attained stable, sustained suppression of flow-induced fluctuations. Moreover, the control strategy demonstrated robustness, effectively reducing fluctuations regardless of the activation phase during oscillations and across multiple reactivation cycles.

In summary, the proposed adaptive control approach proved effective in mitigating fluctuations within the fluid–structure system, significantly stabilizing both the force and the cylinder dynamics. Tangential actuation exhibited particularly strong performance by efficiently modifying wake structures downstream, thereby further enhancing cylinder stability. Although minor fluctuations persisted in the controlled flow, future research should explore methods to eliminate these residual fluctuations entirely and extend the proposed adaptive control to more complex and nonlinear flow systems.

doi:10.6342/NTU202503926

References

[1] J. Chen, Y. Huang, C. Chen, H. Yu, and D. Gao. Review of active control of circular cylinder flow. Ocean Engineering, 258:111840, 2022.

[2] T. Sarpkaya. A critical review of the intrinsic nature of vortex-induced vibrations. Journal of Fluids and Structures, 19(4):389–447, 2004.

[3] C. H. K. Williamson and R. Govardhan. Vortex-induced vibrations. Annu. Rev. Fluid Mech., 36:413–455, 2004.

[4] G. Gómez-de Segura and R. García-Mayoral. Turbulent drag reduction by anisotropic permeable substrates – analysis and direct numerical simulations. Journal of Fluid Mechanics, 875:124–172, 2019.

[5] Qian Mao, Jiazhen Zhao, Yingzheng Liu, and Hyung Jin Sung. Drag reduction by a flexible hairy coating. Journal of Fluid Mechanics, 946:A5, 2022.

[6] Aditya G. Nair, Kunihiko Taira, Bingni W. Brunton, and Steven L. Brunton. Phase-based control of periodic flows. Journal of Fluid Mechanics, 927:A30, 2021.

[7] Reza Maryami and Yu Liu. Cylinder flow and noise control by active base blowing. Journal of Fluid Mechanics, 985:A10, 2024.

[8] J. Rabault, M. Kuchta, A. Jensen, U. Ræglade, and N. Cerardi. Artificial neural

doi:10.6342/NTU202503926

networks trained through deep reinforcement learning discover control strategies for active flow control. J. Fluid Mech., 865:281–302, 2019.

[9] Haokui Jiang and Shunxiang Cao. Reinforcement learning-based active flow control of oscillating cylinder for drag reduction. Physics of Fluids, 35:107140, 2023.

[10] A. Towne, O. T. Schmidt, and T. Colonius. Spectral proper orthogonal decomposition and its relationship to dynamic mode decomposition and resolvent analysis. Journal of Fluid Mechanics, 847:821–867, 2018.

[11] E. A. Deem, L. N. Cattafesta, M. S. Hemati, H. Zhang, C. W. Rowley, and R. Mittal. Adaptive separation control of a laminar boundary layer using online dynamic mode decomposition. Journal of Fluid Mechanics, 903:A21, 2020.

[12] Ching-Te Lin and Hsieh-Chen Tsai. Feedback flow control on a plunging circular cylinder. Physics of Fluids, 36:047126, 2024.

[13] Beverley J. McKeon and Aniruddha S. Sharma. A critical-layer framework for turbulent pipe flow. Journal of Fluid Mechanics, 658:336–382, 2010.

[14] Chi-An Yeh and Kunihiko Taira. Resolvent-analysis-based design of airfoil separation control. Journal of Fluid Mechanics, 867:572–610, 2019.

[15] C. Leclercq, F. Demourant, C. Poussot-Vassal, and D. Sipp. Linear iterative method for closed-loop control of quasiperiodic flows. Journal of Fluid Mechanics, 868:26–65, 2019.

[16] Alessandro Padovan, Samuel E. Otto, and Clarence W. Rowley. Analysis of amplification mechanisms and cross-frequency interactions in nonlinear flows via the harmonic resolvent. Journal of Fluid Mechanics, 900:A14, 2020.

doi:10.6342/NTU202503926

[17] Alessandro Padovan and Clarence W. Rowley. Analysis of the dynamics of subharmonic flow structures via the harmonic resolvent: Application to vortex pairing in an axisymmetric jet. Physical Review Fluids, 7(7):073903, 2022.

[18] C.-T. Lin, M.-L. Tsai, and H.-C. Tsai. Flow control of a plunging cylinder based on resolvent analysis. Journal of Fluid Mechanics, 967:A41, 2023.

[19] W. Yao and R. K. Jaiman. Feedback control of unstable flow and vortex-induced vibration using the eigensystem realization algorithm. Journal of Fluid Mechanics, 827:394–414, 2017.

[20] Feng Ren, Chenglei Wang, and Hui Tang. Active control of vortex-induced vibration of a circular cylinder using machine learning. Physics of Fluids, 31:093601, 2019.

[21] T. McQueen, J. Zhao, J. Sheridan, and M. C. Thompson. Feedback control of flow-induced vibration of a sphere. Journal of Fluid Mechanics, 889:A30, 2020.

[22] Tzu-Yuan Lin, Hsin-Yu Hsieh, and Hsieh-Chen Tsai. A target-fixed immersed-boundary formulation for rigid bodies interacting with fluid flow. Journal of Computational Physics, 429:110003, 2021.

[23] Kunihiko Taira and Tim Colonius. The immersed boundary method: a projection approach. Journal of Computational Physics, 225(2):2118–2137, 2007.

[24] Petros A. Ioannou and Baris Fidan. Adaptive Control Tutorial. Society for Industrial and Applied Mathematics, Philadelphia, PA, 2006.

[25] Andres Goza, Sebastian Liska, Ben Morley, and Tim Colonius. Accurate computation of surface stresses and forces with immersed boundary methods. Journal of Computational Physics, 321:860–873, 2016.

doi:10.6342/NTU202503926

[26] Alexandre M. Roma, Charles S. Peskin, and Marsha J. Berger. An adaptive version of the immersed boundary method. Journal of Computational Physics, 153(2):509–534, 1999.

doi:10.6342/NTU202503926